A Channel Estimation Between a Base Station, Intelligent Reflecting Surface, and a User Equipment

Master's thesis in Communication Engineering

EKATERINA SALTYKOVA

DEPARTMENT OF ELECTRICAL ENGINEERING

CHALMERS UNIVERSITY OF TECHNOLOGY
Gothenburg, Sweden 2023
www.chalmers.se

Master's thesis 2023

A Channel Estimation Between a Base Station, Intelligent Reflecting Surface, and a User Equipment

EKATERINA SALTYKOVA

Department of Electrical Engineering
Chalmers University of Technology
Gothenburg, Sweden 2023

A Channel Estimation between a Base Station,
Intelligent Reflecting Surface, and a User Equipment
EKATERINA SALTYKOVA

Supervisor: Mark Holm, Huawei Technologies
Examiner: Paolo Monti, Department of Electrical Engineering
Advisor: Mohammad Hossein Moghaddam

Master's Thesis 2023
Department of Electrical Engineering
Chalmers University of Technology
SE-412 96 Gothenburg
Telephone +46 76 441 3397

Typeset in LaTeX
Printed by Chalmers Reproservice
Gothenburg, Sweden 2023

A Channel Estimation between a Base Station,
an Intelligent Reflecting Surface, and a User Equipment
EKATERINA SALTYKOVA
Department of Electrical Engineering
Chalmers University of Technology

Abstract

The millimeter-wave (mmWave) spectrum utilized in 5G networks, has enabled massive mobile connectivity with enhanced capacity and data rates, lower latency, expanded coverage, and superior reliability. However, mmWave propagation is vulnerable to higher channel attenuation and increased penetration losses. These adverse effects are especially relevant in dense urban environments like modern cities. A promising solution is the deployment of intelligent reflecting surfaces (IRS), which provide directional transmissions between base stations (BS) and user equipment (UE). As a planar surface consisting of low-cost passive elements, IRS can reflect the incident signal in a controllable way by adjusting the phase shifts of its elements. Currently, the main challenge related to this technology is the difficulty in acquiring the channel state information (CSI) between the BS, the IRS, and the UE. Knowledge of CSI is essential for configuring the IRS. Instead of conventional channel estimation, this thesis proposes a novel approach for spatial channel estimation based on retrieving an angular position of the UE, in terms of azimuth and elevation angles, relative to the IRS. For acquiring this data, it is suggested to apply monopulse radar principles and implement a monopulse beamforming technique on the IRS side. The phase shifts of the IRS's elements can be optimized accordingly to the evaluated spatial information to redirect the signal sent from the BS to the UE. This thesis introduces and tests an algorithm for estimating the UE's location relative to the IRS based on the amplitude-comparison monopulse detection technique. Several IRS configurations are examined, and their performance is analyzed. The accuracy of the proposed algorithm for different IRS configurations is evaluated. It is shown that the monopulse beamforming technique can be integrated into the BS-IRS-UE setup to determine the UE's angular coordinates. Numerical results reveal that the estimation accuracy improves by narrowing the monopulse patterns widths, which is achieved by increasing the number of scattering elements that the IRS consists of.

Keywords: mmWave, IRS, spatial channel estimation, monopulse beamforming, amplitude-comparison monopulse

Acknowledgements

I would like to acknowledge and give my warmest thanks to my supervisor Mark Holm for the great support and guidance he has provided me throughout the project. His continuous assistance and knowledge-sharing carried me through all the stages of writing this thesis and helped me successfully finalize it. I am also very grateful to Srikanth Gopal from Huawei Technologies for his generous advisory and for giving feedback on all the technical matters related to the subject of this work. Finally, I want to thank Huawei Technologies for providing me with the opportunity to work in its research unit in Gothenburg and collaborate with brilliant engineers on the research topic.
To my family and partner, I want to express my special gratitude for making it possible for me to study abroad and for your enormous support throughout this journey.

Ekaterina Saltykova, Gothenburg, June 2022

List of Acronyms

Below is the list of acronyms that have been used throughout this thesis listed in alphabetical order:

AAU	Active Antenna Unit
ADC	Analog-to-Digital Converters
AoA	Angle of Arrival
AoD	Angle of Departure
AP	Access Point
BS	Base Station
CG	Coffee-Grinder Channel Model
CSI	Channel State Information
DOA	Direction of Arrival
DBF	Digital Beamforming
EE	Energy Efficiency
EM	Electromagnetic
eMBB	Enhanced Mobile Broadband
FD	Full Duplex
FOV	Field of View
FPGA	Field-Programmable Gate Array
ICI	Inter-Cell Interference
IRS	Intelligent Reflecting Surface
LOS	Line-of-Sight
MBS	mmWave Base stations
MIMO	Multiple-Input and Multiple-Output
NLOS	Non-Line-of-Sight
OFDM	Orthogonal Frequency-Division Multiplexing
PIN	Positive-Intrinsic-Negative
PV	Photovoltaic
RAN	Radio Access Networks
RES	Renewable-based Energy Sources
RF	Radio Frequency
RRU	Remote Radio Unit
Rx	Reception
RX	Receivers
SE	Spectral Efficiency
SNIR	Signal-to-Interference-Plus-Noise Ratio
UE	User Equipment
Tx	Transmission
TX	Transmitters
TDMI	Time Division Monopulse Interleaving

Contents

List of Figures

List of Tables

1
Introduction

1.1 Background

The last two decades have introduced significant technological advancements in wireless communications, facilitated by the constant demand for high-quality and ubiquitous wireless services [1]. Scientists and engineers constantly seek ways to optimize wireless communication systems to support an increasing number of users and devices. To this end, a variety of techniques have been introduced to leverage the maximum theoretical capacity of wireless networks, ranging from new waveforms, multiplexing techniques (e.g. OFDM), multipath propagation (e.g. MIMO) exploitation, and advanced modulation and coding techniques. Cellular network infrastructure has become denser, and new techniques have been developed to coordinate intercellular communication and deal with network interference issues. However, significant capacity limitations of the wireless networks come from the unreliability of the wireless propagation environment and spectrum shortage [2]. Wireless communications utilize frequency bands extending from hundreds of megahertz (MHz) to a few gigahertz (GHz). This spectrum range shows favorable propagation characteristics and allows the implementation of efficient and low-cost transceivers.

Nonetheless, the need to increase data capacity has resulted in a shift into higher frequency bands to exploit previously unused spectrum, known as millimeter-wave spectrum. This spectrum is planned to be utilized in the fifth generation of wireless mobile networking technology (5G). Previously, frequency bands above 10GHz were considered unsuitable for enhanced mobile broadband (eMBB) communications due to the variety of challenges they pose. These frequencies are associated with high attenuation and dominance of first-order reflections and scattering, making it considerably more hostile than the channel at sub-6 GHz frequencies. Moreover, the mm-wave spectrum is spatially sparse, limiting the number of available propagation paths between transmitter and receiver and, hence, decreasing the number of spatial data streams supported by the channel [2]. This poses a challenge to the channel spatial multiplexing capability, which is more feasible in sub-6 GHz channels. The abovementioned complications are particularly relevant for cluttered, dense urban environments, where wireless transmissions frequently require non-line-of-sight (NLOS) links. Even though some methods and techniques, such as the widespread installation of mmWave base stations (MBSs), or the usage of directional high-gain antenna arrays combined with adaptive beamforming, can enhance coverage and overall reliability of the wireless channel, they can also introduce new issues like inter-cell interference (ICI), which severely affects the communication quality of the cell-edge users [3] [4]. Thus, there is still a need to develop new technologies that will contribute to the achievement of the continuous capacity growth of future wireless communications [5].

Intelligent reflecting surface (IRS) has recently been introduced as a promising technique for the performance optimization of wireless communication networks. The IRS is a digitally controlled planar surface composed of many low-cost passive reflecting elements, each being capable of independently making a change to the amplitude and phase of the incident signals [6]. By adjusting reflecting coefficients, IRS can advantageously reconfigure the wireless propagation environment. In particular, the signal reflected by the IRS can be added coherently to the signals propagating through other paths, thereby enhancing the power of the received signal or combined with them in a destructive manner to reduce interference. Considering the IRS's design and the flexibility of its deployment, this new technology has an appealing advantage over traditional relaying communication. It has the potential of reducing hardware costs and decreasing energy consumption, as well as facilitating NLOS communication, which will significantly improve the 5G network coverage.

1.2 Purpose

One of the challenges related to the IRS deployment is the estimation of the channel between the Base Station (BS), the IRS, and the user equipment (UE). It is critical to know accurate channel state information (CSI) to exploit the IRS's potential in wireless communications fully. Therefore, an effective channel estimation strategy should be developed. However, acquiring CSI is not a trivial task, mainly due to two factors: the IRS's passive nature and the uncontrollability and randomness of the radio propagation environment. Up to now, numerous research works have been published that explored various approaches for channel estimation in IRS-aided mmWave communication. A more comprehensive overview of the proposed strategies is done in the theoretical part of the report. Nonetheless, it is worth saying that no approach has been standardized as of yet.

This thesis aims to propose and test a new methodology for spatial channel estimation of IRS-aided wireless links. Instead of the conventional CSI acquisition techniques, this study suggests exploiting the principles of the monopulse radar, which finds its origin in tracking systems, and implementing a monopulse beamforming technique at the IRS side to acquire spatial information of the UE in terms of azimuth and elevation angles. Based on this information, the phase shifts of the IRS's components can be adjusted accordingly to provide a communication link between the BS and the UE.

1.3 Limitations

Due to the complexity of the research topic and given time constraints, this study has a few limitations. First, only a stationary channel between the IRS and the UE is considered. Secondly, the study only examines the case of determining the angular location of one UE at a time. This limitation is related to the monopulse technique, which does not allow tracking multiple targets simultaneously.

1.4 Societal, Ethical and Ecological Aspects

The deployment of the 5G networks is already rapidly transforming not only the telecommunication industry but also other major economic sectors, like manufacturing, transportation, healthcare, and education. 5G technology promises to revolutionize our ways of living, working, and interacting with each other. However, the adaptation of this technology into our everyday life must be made in a sustainable and responsible way, taking into account its potential environmental and social impacts.

Overall, 5G has the potential to contribute significantly to sustainability goals, particularly in areas such as e-health, smart manufacturing, sustainable transportation, and affordable, high-quality education. 5G can transform healthcare by enabling remote diagnostics, monitoring, and treatment of patients in real time, which would be especially beneficial to those living in remote areas and having difficulties accessing medical care. 5G can drive innovations in manufacturing industries, by facilitating the use of advanced robotics and automation, enabling the possibility of real-time monitoring and analysis of production processes. This eases the identification of production issues in the early stage, which can decrease downtime, improve efficiency, and lead to cost savings. Production automatization can as well enable predictive maintenance, helping to avoid equipment failures and reducing maintenance costs. 5G can improve transportation by enabling the production of autonomous vehicles and enhancing traffic management systems, which can benefit the overall safety of the roads and help with optimizing transportation networks to reduce idling time, traffic congestion, and fuel consumption. 5G can contribute to providing high-quality education by enabling new learning experiences, for example, by introducing immersive virtual and augmented reality, which offers students learning in a more interactive and engaged way. Also, 5G can expand access to education by providing the possibility of remote learning experiences without experiencing connectivity issues and delays and increasing the number of educational resources which can be accessed quickly and efficiently.

However, as with any new technology, there are several potential downsides that should be considered. There are concerns related to privacy and security, as enhanced connectivity and data transfer can make personal and sensitive information more vulnerable to various malicious attacks, jeopardizing overall networking safety. The level of automation and AI enhancement facilitated by 5G raises ethical considerations on job displacement, widespread surveillance, and collection of private data.

In addition, one major concern that arises with the emergence of 5G wireless networks is how efficient they can be in terms of energy consumption. In fact, from both cost and carbon footprint perspectives, the energy consumption of mobile wireless networks is one of the industry's biggest challenges. Typically, the major contribution to the excessive energy consumption in mobile networks comes from the Radio Access Networks (RAN) and radio base station sites. A single 5G base station with 128 active antenna units (AAU) will consume almost twice as much power compared to a base station deploying a 4G remote radio unit (RRU) [7]. A number of new, power-hungry parts, including mm-wave transceivers, field-programmable gate arrays (FPGAs), quicker data converters, high-power or low-noise amplifiers, and integrated Massive MIMO antennas, are expected to be deployed at the 5G base station site. Additionally, the 5G network requires a higher number of base stations compared to the 4G network, which also contributes to the overall increase in power and energy consumption.

The joint use of multiple approaches can resolve the energy challenge: the use of renewable energy sources, the application of the "sleeping mode" during which the active electronic components of the BS are turned off during times of no traffic, or the densification of the mobile network through IRSs. As was mentioned before, one of the primary use cases of the IRS is coverage enhancement by creating additional paths for UEs with a blocked direct line of sight (LOS) to BSs. As the IRS consists mainly of passive elements, it has a great potential to decrease the overall energy consumption throughout the whole network while preserving performance and coverage. Thus, the IRS can potentially reduce telecom systems' energy consumption, thereby contributing to meeting global sustainability goals.

1.5 Thesis Outline

This thesis consists of six chapters. Following the Introduction, Chapter 2 details the theoretical aspects of the IRS and the monopulse radar. Chapter 3 presents and explains the methodology used in the research. Chapter 4 elaborates on the results, combining them with a discussion of the research findings. Chapter 5 provides a conclusion to the thesis work and is followed by reflections on avenues for future research in Chapter 6.

2
Theory

This chapter provides a theoretical overview of the working principles of the IRS and the monopulse radar. The IRS subsection highlights the basic features of the technology, discusses its potential benefits and use case scenarios, and outlines some practical challenges. The subsection dedicated to the monopulse radar explains the monopulse concept and overviews two main monopulse techniques: amplitude-comparison monopulse and phase-comparison monopulse.

2.1 Intelligent Reflecting Surface (IRS)

A novel technology, Intelligent Reflecting Surface (IRS) or Reconfigurable Intelligent Surface (RIS), has recently appeared on the market and is gaining traction in the scientific community. The IRS is a planar surface comprised of arrays of passive scattering elements. Each element is controlled in a software-defined manner and is used for modifying the electromagnetic (EM) properties, like a phase shift, of the reflection of the incident signals [8]. This kind of reflection does not follow Snell's law, i.e. the angle of incidence is not equal to the angle of reflection. Therefore, it is usually referred to as anomalous reflection [9].

Dense deployment of IRSs and sophisticated coordination of their reflections could alleviate adverse propagation phenomena of the wireless environment, such as multi-path fading, signal path loss, and co-channel interference, hence improving communication performance. For example, if there are no LOS communication links, IRSs aid directional transmissions by forming virtual LOS channels between base stations and end users. It resembles conventional beamforming when delayed copies of the same signal are emitted from multiple antennas [8], creating a directional beam towards the receiver. Time delays are introduced to the signal scattered from the surface by adjusting each of the IRS elements' phase shifts to facilitate the constructive interference of EM waves toward the UE's direction; in other words, passive beamforming is being carried out.

2.1.1 Benefits of IRS-aided Wireless Communication

Constructing the wireless environment with the prevalence of LOS links between BSs and UE results in achieving more desirable propagation characteristics in the millimeter-wave band, such as enhanced energy or spectral efficiency (EE/SE) and signal-to-interference-plus-noise ratio (SINR), compensated path loss (propagation and penetration losses combined), improved network capacity and extended network coverage. Other practical advantages of the IRS include its passive nature. In an ideal case, the surface consists of reflecting elements that passively redirect the impinging signal without amplification; thus, there is no need to mount any radiofrequency chains (RF) for transmitting or/and receiving signals [5]. Such a structure makes the hardware design less complex and decreases the device's energy consumption compared to the traditional active antenna arrays or relays. Another benefit is that the IRS can support real-time communications as it operates as a passive full-duplex (FD) repeater. Additionally, compatibility with already existing standards and hardware of wireless networks makes IRS-enhanced communications a favourable solution for 5G wireless standard challenges [10].

2.1.2 IRS's Architecture and Control Mechanism

IRSs are typically considered two-dimensional metasurfaces, i.e. having a near-zero thickness, that comprises a large number of sub-wavelength-scaled reflecting elements. The structural arrangement of the IRS elements determines the resulting transformation of the impinging EM waves, i.e. directivity and intensity of the reflected and diffracted waves [11]. In general, the IRS's reconfigurability is defined by its ability to jointly control the phase of its elements in order to achieve the desired EM behaviour of the reflected waves (e.g. wireless signals). It is often assumed that no coupling occurs in the reflection of the adjacent IRS elements, meaning that each of the elements reflects the signal of interest independently. Therefore, the resulting signal formed via the IRS is the superposition of all the EM waves reflected from the corresponding IRS elements. In wireless communication, the propagation channel is time-varying. Thus, the IRS should be able to adjust its response in real time based on the channel variation [5]. Hence, it implies that the IRS elements should be manufactured to enable dynamic tuning of the IRS elements' reflection coefficients.

Over the past years, various IRS architectures have been proposed. Based on a few of them, a generalized IRS architecture is compiled and demonstrated in Figure 2.1. Typically, the IRS is composed of three layers. The outside layer comprises N reconfigurable patches printed on the dielectric wafer. These patches are a combination of tunable chips, which interact locally with scattering elements and a central controller [12] [13]. The central controller establishes a software-defined realization of a control mechanism defining the IRS's ability to dynamically reconfigure its EM behaviours [14]. The middle layer deploys a copper plate which minimizes the leakage of the signal's energy during the IRS's operation. The interior layer represents a control circuit board that controls the state of the IRS elements and tunes their reflection phase shifts [5].

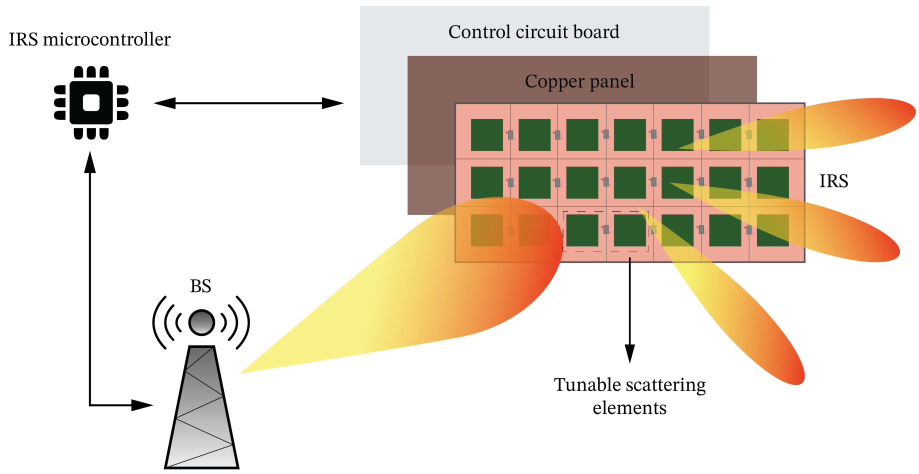

Figure 2.1: A hardware architecture of the IRS.

Usually, tunable chips are electronic devices, like positive-intrinsic-negative (PIN) or varactor diodes [13] [15]. However, other approaches for controlling the IRS elements' reflections have also been examined, like in research work by Senglee Foo [16]. The author proposes using electronically controllable liquid crystal, which is loaded as a thin layer in each of the IRS's cells. Via controlling the voltage bias on each cell, the effective dielectric constant of the liquid crystal material will change, resulting in desirable phase shifts across IRS. Nonetheless, the most prevailing widely adopted approach for tuning the IRS elements is based on the implementation of PIN diodes, characterized by fast response time and comparatively low energy consumption. Different biasing voltages are applied to the PIN diode via a direct-current (DC) feeding line, and the PIN diode switches between the ON and OFF states, which results in an induction of a phase-shift difference of π to the incident signal [5]. Typically, the reflection coefficient magnitude of each element is set as large as possible within the range (0,1]. In [17], [18], it was shown that for IRS with a large number of reflecting elements, it is more practical and cost-effective to apply only discrete and finite phase-shift levels (e.g. 0 or π), which requires a small number of control bits (e.g. 0 or 1). Although continuous tuning of the reflection coefficients seems more beneficial for optimizing the communication performance, it is more challenging to implement since higher resolution reflecting elements demand increased hardware complexity and, hence, higher cost. Figure 2.2 provides a schematic look of the IRS's unit cell, consisting of two scattering elements and the tunable chip (e.g. a varactor or PIN diode) incorporated in between them to provide a variable impedance. The basic topology and dimension parameters of the IRS's scattering elements (d_x, d_y, x_0, y_0, z_0, g_0) can be optimized to enable IRS operation in different frequency ranges [11].

The IRS controller is responsible for altering the state of the tunable chips and, hence, determining the IRS reflection adaptation. Also, the IRS controller serves as a gateway between the IRS and other network components (e.g. BSs). It receives configuration requests and calibrates the tunable chips for reconfiguring the corresponding scattering elements' behaviour, enabling anomalous reflection, beam steering, and beamforming [11]. One of the typical implementations of the IRS controller is via field-programmable gate arrays (FPGA). The controller can be connected to external devices through wired or wireless backhaul links [5].

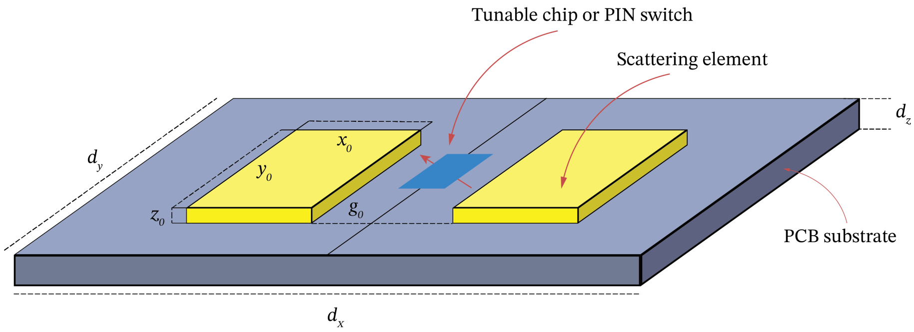

Figure 2.2: Schematic representation of the IRS's unit cell.

It can be noted that even though the IRS is referred to as passive, it requires a power source for controlling the reconfigurability of its reflecting elements and sustaining the operation of its controller. However, this power consumption is considerably lower than that of active antenna arrays (e.g. massive MIMO or multi-antenna relays). Therefore, it can be practically neglected for comparison [19], [20].

2.1.3 IRS's Application in Wireless Networks

Numerous research works are investigating the potential enhancement of IRS-assisted wireless communication. The most frequently encountered improvements include maximization of signal-to-noise ratio (SNR) and overall EE/SE, interference suppression, minimization of transmit power, and lowering physical layer security risks.

The authors in [21] show the improvement of the received signal power at the UE by deploying one IRS with N passive scattering elements to assist the downlink communication in a multiple-input single-output (MISO) system. It is proposed to optimize the BS's transmit beamforming and the IRS's reflection adaptation to maximize the SNR. The authors propose to employ alternating optimization for adjusting active and passive beamforming strategies in an iterative manner. Considering the IRS's passive beamforming, the maximum-ratio transmission strategy is proposed to obtain the BS's optimal beamforming. The IRS's passive beamforming is aligned with the direct channel to boost the received signal power. Numerical results show that compared to non-IRS-assisted MISO systems, the SNR at the receiver increases in the order of N^2 when IRS is used. The study [22] is investigating the application of multiple IRSs to assist wireless mmWave MISO communications. It is presented that through joint optimization of active and passive beamforming, the IRS can increase the received signal power and extend network coverage by providing alternative signal paths. The authors also study the power scaling law obtained in [21] and reveal that the SNR indeed increases quadratically with the number of IRS's scattering elements.

Besides the potential enhancement of the SNR, the IRS can aid in reducing the BS's transmit power and overall maximization of EE/SE performance [11]. Considering the reduction of the BS's power consumption with the maintenance of the same level of transmission performance, it is possible to think of IRS-aided wireless communications as a green technology for wireless networks in the near future. Authors of [23] focus on the downlink transmissions in the IRS-assisted multiuser MISO system as in [21], and devise an algorithm for minimizing the BS's transmit power under individual users' SINR constraints. They investigate the semidefinite relaxation (SDR) procedure for beamforming optimization and the alternating optimization algorithm, which suggests the iterative optimization of the BS's transmit beamforming direction and transmit power and the IRS's phase shifts until the convergence is achieved. Numerical results demonstrate that the BS's transmit power can be scaled down in the order of $1/N^2$ while the SNR at the receiver is not compromised.

Several studies examine the IRS's application for suppressing inter-cell interference and assisting the communication performance of cell-edge users. For instance, in [24], the maximization of the minimum weighted SINR in a multi-cell MISO system is achieved by applying the techniques of second-order-cone programming (SOCP) and SDR for optimizing transmit and reflective beamforming. The authors also further suggest an algorithm based on the principle of successive convex approximation (SCA) for tackling the beamforming optimization problem, which requires less computational complexity. Numerical results reveal that the proposed algorithm can noticeably increase a min-weighted-SINR in IRS-aided communications compared to conventional cases without the IRS.

In addition, some papers prove the that the secrecy rates of the physical layer can be improved in IRS-assisted systems. By adapting the IRS's reflection coefficients, it is feasible to simultaneously create enhanced directive beams toward the intended receiver and suppress beams toward the unintended user, like an eavesdropper. Driven by the idea of securing physical layer communications from eavesdropper attacks, the authors in [25] examine the IRS potential in wireless MISO systems with a presence of an eavesdropper. The IRS is placed next to a legitimate receiver (LR). By sophisticated optimization of both the IRS and legitimate transceiver (LT) beamformer, it is possible to prevent the eavesdropper's malicious intentions. Therefore, the secrecy rate at the LR, defined by the amount of information securely sent over a wireless communication channel per time unit [26], can be enhanced.

Overall, the IRS has the potential to become an effective tool for improving future wireless communications by reconfiguring signal reflections in an uncontrollable wireless channel in favor of network performance optimization [11]. Moreover, the IRS can be easily integrated into the urban propagation environment due to its relatively modest dimensions, i.e. in the outdoor environment, it can be coated on the building facades, billboards, lamp posts, etc., and in an indoor environment, it can be mounted to ceilings, walls, or even some furniture.

2.1.4 Challenges Related to IRS

It is worth mentioning that all of the research works mentioned above [21]-[26], which reap the benefits of IRS-aided wireless communication by joint optimization of the transmit and passive beamforming, assume perfect knowledge of CSI. In general, the ability to optimize the IRS elements' configuration depends on the available information of all channels considered. At least partial knowledge about the propagation environment is required for the IRS to be reconfigured appropriately and effectively improve system performance [2]. Therefore, accurate CSI acquisition of the relative IRS-reflected links is crucial. However, it is a rather challenging task due to the lack of sensing capabilities at the IRS, which is a passive component. Additionally, the large number of scattering elements it comprises leads to a proportional amount of channel parameters to be estimated, which results in a large overhead for estimation. Therefore, conventional channel estimation methods are not feasible, and new approaches to solving this issue should be devised.

Up to this point, numerous studies have been conducted on channel estimation in IRS-assisted wireless communication systems. The existing methods for CSI acquisition can be generally subdivided into two categories: explicit CSI acquisition, i.e. channel estimation, and implicit CSI acquisition, i.e. beam training [27].

For the explicit channel estimation, the sequence of pilot signals is sent from the BS to the UE or vice versa through downlink/uplink IRS-aided wireless channels. The channel estimation happens either at the BS or the UE side. There are two approaches overviewed in research works for obtaining CSI with the IRS based on the two different IRS architectures.

The first approach implies a semi-passive IRS, i.e. the IRS is equipped with additional sensing devices operated by low-cost receive RF chains, enabling the capability of processing the sensed signal. Based on [28]-[29], a transmission protocol for the semi-passive IRS can be described as follows: firstly, the IRS is operating in a sensing mode with all the sensing elements being ON, whereas reflecting elements are turned OFF. During this phase, the BS and the UE exchange pilot signals for estimating respective BS-IRS and IRS-UE channels. Afterwards, the IRS exchanges the received CSI with the BS, based on which the active and passive beamforming is jointly optimized. Finally, data transmission between the BS and the UE starts, and the IRS switches to the reflection mode to enhance uplink/downlink communication. This approach provides only limited CSI, which might not be enough for initializing beamforming with the high SNR. Hence additional techniques like compressed sensing and deep learning tools might be required to construct the full channel knowledge. Additionally, this approach contradicts the motivation for adding the IRS to mobile network systems, increasing hardware complexity, cost, and power consumption.

The second approach exploits only the passive IRS. In this case, only cascaded channels, i.e. BS-IRS-UE, can be estimated either at the BS or the UE side in the uplink or downlink, respectively. The transmission protocol also consists of three consecutive phases: firstly, either the BS or the UE transmits orthogonal pilots to each other, while the IRS varies its pre-defined reflection pattern. At the same time, the BS or the UE performs estimation of both the BS-UE direct channels and the BS-IRS-UE cascaded channels. Following this, CSI is fed to the BS, and it in turn jointly configures the IRS reflection coefficients for transmitting data with its active beamforming. The configured reflection pattern is sent to the IRS controller via the backhaul link. Finally, the IRS adjusts its reflection coefficients accordingly to assist data exchange between the BS and the UE. Authors in [30] and [31] propose the ON/OFF based least square (LS) IRS reflection pattern, which is derived from the successive estimation of the cascaded BS-IRS-UE links. The algorithm implies that only one reflection element is activated at each given time slot. Thereby, the direct BS-UE channel and cascaded channels formed via different IRS elements are estimated separately. Despite the simplicity of the implementation, the IRS reflection pattern created via this method suffers significant reflection power loss since only one IRS element is turned on at a time, resulting in a weak reflected signal. Instead of using the ON/OFF strategy, authors in [32] suggest an approach that determines the reflecting coefficient matrix based on the discrete Fourier transform (DFT) matrix and uses a minimal variance unbiased (MVU) estimator for estimating the channel coefficients. The estimation error produced by this technique is typically significantly less than that produced by the ON/OFF strategy. Also, there are other papers proposing further enhancement of CSI acquisition in IRS-aided communications, like reduction of pilot overhead by grouping adjacent IRS elements [33], compressive sensing [34], and application of deep-learning tools [35].

The second category of CSI acquisition implies beam training, where instant CSI is obtained by estimating relevant physical parameters of the propagation paths, including the angle of arrival (AoA), the angle of departure (AoD), and path gain. The beam training in IRS-assisted systems is based on designing a codebook that defines multiple IRS directional beams, which is used for searching for the optimal beam in the spatial domain between the IRS and the UE, yielding the optimal performance [**5**]. However, in IRS-assisted systems, it is impractical to use traditional beam training methods such as an exhaustive search during which all the possible combinations of transmitter-receiver beam pairs are jointly examined until the dominant path is determined. This method will incur unacceptably high training overhead in IRS-aided communications due to a large number of the IRS's scattering elements. To address this issue, authors in [36] examine a novel multi-beam beam training method, the essence of which is the division of the IRS reflecting elements into multiple subarrays and designing the corresponding multi-beam steering over time. The UE can identify the efficient beam by comparing the signal power over time. This method has a promising potential to reduce the training overhead and keep beamforming performance for data transmission at a decent level. Furthermore, beam training can be facilitated by means of machine learning algorithms, though such approaches are still at an initial stage of research.

Even though there is already a variety of research papers devoted to the issue of CSI acquisition in IRS-assisted wireless networks, a search for a practically efficient channel estimation method that would guarantee to achieve high accuracy and lower training overhead, is still open and remains an important issue in the IRS-related research area.

2.2 Monopulse Radar

This thesis aims to suggest and test a new approach for optimizing the configuration of the IRS components based on the prior retrieved information about the UE's angular location. This method for spatial channel estimation belongs to the implicit CSI acquisition category and originates from the techniques applied in the tracking radar systems. It is proposed to implement a monopulse beamforming technique at the IRS for evaluating the angle components of the UE, i.e. elevation and azimuth angles, relative to the IRS. Based on this data, the IRS reflection coefficients can be set appropriately to assist a transmission link between the BS and the UE.

2.2.1 Monopulse Concept

Radars can be divided into two categories: search radars and tracking radars. Search radars are exploited for locating targets within significant volumes of space. The target information received is the range, i.e. distance to the target, azimuth, and elevation angles of the target. The azimuth angle provides the object's angular position around the horizon, whereas the elevation angle, sometimes referred to as altitude, is the angle between the horizon and the object. Angular measurements are shown in Figure 2.3. Tracking radars are used for following the spatial position of one or multiple targets in space. Typically, such radars have a highly directional antenna pattern, i.e. they radiate a relatively narrow beam. They provide accurate information about the target, such as range, angular position in terms of azimuth and elevation angular coordinates, and Doppler frequency shift if required by the application purpose. Tracking radars can be classified into three categories depending on which technique is applied to obtain the target's location relative to the radar beam. These techniques are sequential lobing or beam switching, conical scanning, and monopulse tracking [37]. However, monopulse tracking is more advantageous than the other two techniques since it avoids problems present in conical scanning or lobe switching radar systems, such as low tracking accuracy due to the target scintillation and high vulnerability for jamming.

The term monopulse originates from the ability of the system to extract the range and angular coordinates of the target from only one signal pulse. A radar system's transmitter generates pulses of electromagnetic (EM) radiation at a regular rate, which is radiated by the radar's antenna toward the potential direction of the target. If the target is in the propagation direction of the transmitted signal, this EM energy will be reflected from the target's surface and will travel back to the receiver. The receiver processing unit analyzes the received echo, and the target's location

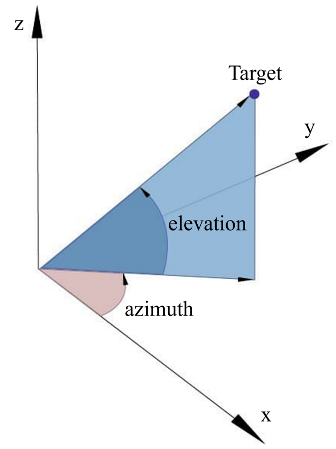

Figure 2.3: Schematic representation of the azimuth and elevation angles.

and properties are derived. In classical monopulse systems, the radar beam pattern is split into two (or more) parts, and then the two (or more) resulting signals are sent out of the radar. After receiving the reflected signals, they are amplified separately and compared. The direction with the strongest return indicates the general target's direction relative to radar boresight.

Overall, the following definition of a monopulse radar can be considered: a monopulse radar is a radar system that obtains the angular location of a target by comparing signals originating from the same transmitted pulse received simultaneously in two or more antenna patterns. In contrast, techniques such as conical scanning and lobe switching derive angle information from a series of sequential antenna receive patterns [37]. The main advantage of the monopulse technique is that the target's echo amplitude fluctuations do not affect the accuracy of the measurements, as the angular information is derived during one signal pulse, which is generally a few microseconds [38].

There are two types of monopulse tracking radars depending on the monopulse detection technique: amplitude-comparison and phase-comparison. In amplitude-comparison monopulse, two or more radar beams originate from the same phase center of the radar's antenna unit. Hence, for every direction of arrival, an amplitude difference of the signal received from both beams will measure the target's angular displacement. In phase-comparison monopulse, the beams are parallel to each other and originate from slightly shifted phase centers [39]. Therefore, the target's angular information is extracted from the phase difference of the received signals occurring due to the target's angular location relative to the receiver. The target is assumed to be in the far-field region. The working principles and properties of both methods will be discussed thoroughly in the following subsections.

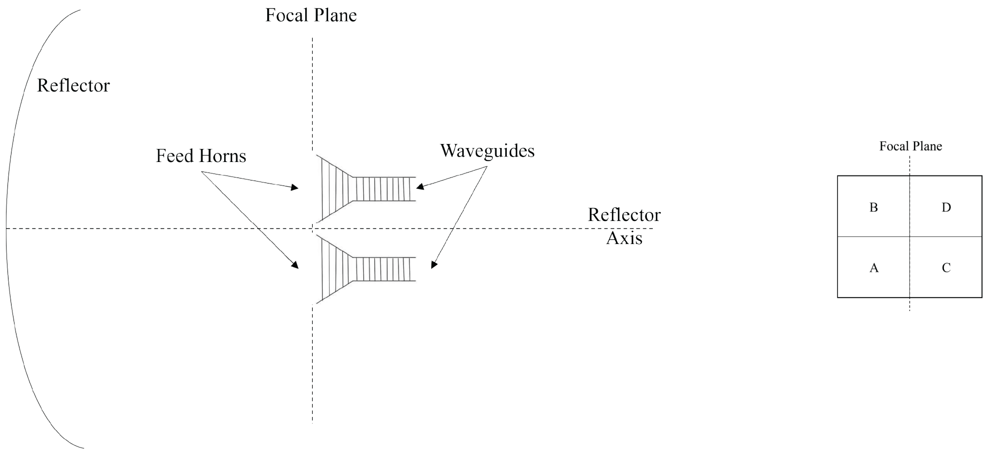

Figure 2.4: The side view of the monopulse radar's reflector and feed horns, and the axial view of the feed horns from the reflector perspective.

2.2.2 Amplitude-Comparison Monopulse

This section presents an example of one of the various forms of monopulse radar configurations. This idealized model represents the basic principles of the radar belonging to the amplitude-comparison monopulse category. Generally, monopulse radar systems can be deployed with reflector antennas, lens antennas, or array antennas [38].
In the model presented in Figure 2.4, the monopulse radar is constructed from a parabolic-reflector antenna fed by a block of four feed horns placed symmetrically in the focal plane. This type of antenna is commonly used in mechanically steered monopulse radars [37]. The lefthand side of Figure 2.4 shows a side view of the structure, and only two horns displaced on one side of the reflector axis, i.e. the boresight axis, are visible. In contrast, the other two are displaced in the opposite direction. The righthand side of Figure 2.4 demonstrates an axial view of feed horns from the reflector perspective. The four feed horns are required to retrieve the two angle components, i.e. azimuth and elevation, relative to the boresight axis of the radar simultaneously.

These horns produce four squinted beams, as illustrated in Figure 2.5a. Their patterns overlap, and the main beam directions are squinted at a particular angle θ. Worth noticing that the upper beams are produced by the lower horns [37]. As it was mentioned earlier, the four beams originate from the same phase center, so their responses to the incident plane wave, i.e. radiation pattern coming from a target, would be in the same phase but mainly vary in amplitude in accordance with the beam patterns and the wave's direction-of-arrival (DoA). Figure 2.5b shows the cross-section of the four monopulse antenna beams.

Figure 2.6 demonstrates the basic principles of the amplitude-monopulse method for estimating one of the angle coordinates, i.e. either azimuth or elevation, with one antenna and two feed horns in use. The two received signals have the same phase but differ in amplitude, referred to as Δx_1 and Δx_2 in Figure 2.6.

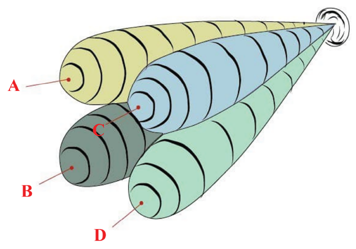

(a) Four squinted beams produced by monopulse radar's horns.

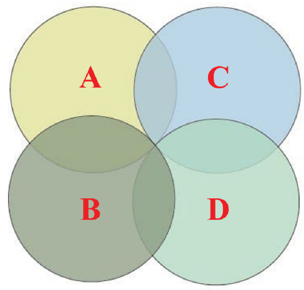

(b) The cross-section of the four squinted beams.

Figure 2.5: Illustration of the monopulse antenna beams.

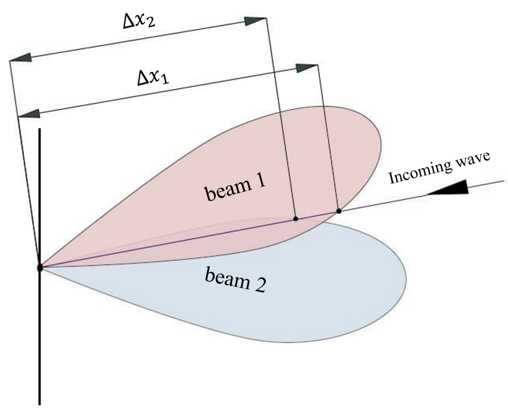

Figure 2.6: Schematic representation of the amplitude-comparison monopulse technique principles.

For performing monopulse processing to estimate the DoA of the target, the monopulse radar system switches between the two modes: transmission (Tx) and reception (Rx). In Tx mode, the four beams emanating from the radar's antenna unit are combined into a sum beam or a sum pattern, denoted by $\sum$. The sum pattern is a pencil beam with its peak on the boresight axes, and it is used for target detection. In Rx mode, the EM wave coming from the target is received through four receive beams, and their outputs' voltages, i.e. signal amplitudes, are obtained. Note that the receive beams are squinted to slightly different angles relative to the transmit beam. Afterwards, sum patterns and two difference or delta patterns, denoted as Δ, are acquired from these voltages. The two delta patterns are azimuth, denoted as Δ_{az}, and elevation, denoted as Δ_{el} [16]. The way the monopulse radar system forms the sum and difference patterns can be referred to as monopulse beamforming. The four received voltages correspond to A, B, C, and D beam patterns shown in Figure

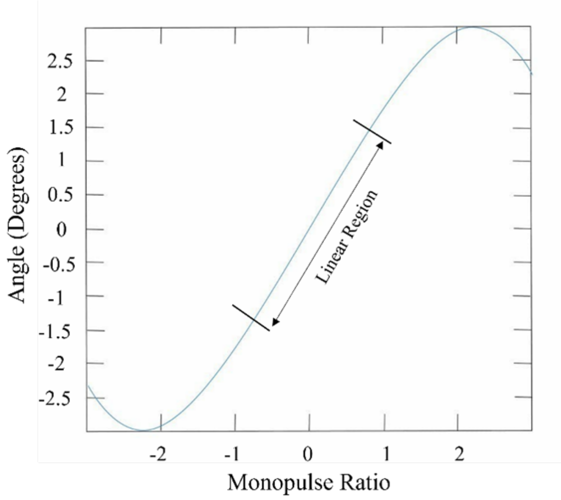

Figure 2.7: The curve of the monopulse ratio.

2.5b. The beam patterns $\sum$, Δ_{az}, and Δ_{el} are then calculated as [1]:

$$\textbf{Sum} \quad \Sigma = (A + B + C + D) \tag{2.1a}$$

$$\textbf{Azimuth difference} \quad \Delta_{az} = (C + D) - (A + B) \tag{2.1b}$$

$$\textbf{Elevation difference} \quad \Delta_{el} = (A + C) - (B + D) \tag{2.1c}$$

The sum pattern is maximized by the monopulse boresight axes, i.e. where four antenna patterns overlap. In contrast, the azimuth and elevation difference patterns both have their nulls in the boresight direction. This means that the maximum sum pattern output will be obtained if the target is located precisely on the antenna's boresight axis, whereas the difference pattern will be equal to zero.

The sum and difference patterns are used to calculate the so-called monopulse ratio, or error signal, representing the difference between the antenna pointing direction and target direction [40]. These are defined as

$$e_{az} = \mathrm{Re}(\frac{\Delta_{az}}{\Sigma} \cos \delta_{az}) \tag{2.2a}$$

$$e_{el} = \mathrm{Re}(\frac{\Delta_{el}}{\Sigma} \cos \delta_{el}) \tag{2.2b}$$

where Δ_{az} and Δ_{el} refer to the magnitudes of azimuth and elevation difference patterns, whereas δ_{az} and δ_{el} refer to the phase angle of sum and azimuth or elevation difference patterns. If the two directions coincide, then the error signal equals zero. The sum pattern is used to normalize the difference patterns to make the error ratio (e_{az}, e_{el}) independent of the signal amplitude related to the size of the target return.

An exemplification of the monopulse ratio is shown in Figure 2.7. As an idealized model of a monopulse is considered, it is assumed that the $\sum$ and Δ always have 0°

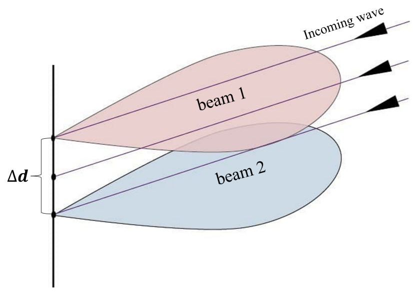

(a) Illustration of the phase-comparison monopulse receive beams originating from the two antennas.

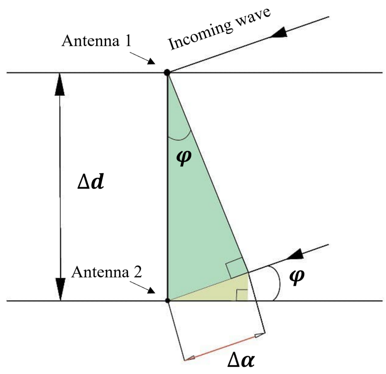

(b) Geometrical principles of the monopulse phase-comparison.

Figure 2.8: Schematic representation of the phase-comparison monopulse technique principles.

or 180° relative phase due to them being derived from four individual beams placed at the same phase center, i.e. their outputs have the same phase [37]. Therefore, if the target is located on one side of the boresight axis, the cosine is equal to +1, and it is −1 if the target is on the opposite side.

The sum and difference magnitudes ratio indicates how far the target is off the monopulse axes. At the same time, the cosine factor specifies the target's location relative to the axes, i.e. above or below the axes, left or right of the axes.

The error signal output is used for adjusting the position of the mechanically steered tracking radar so its boresight axis aligns with the target position [38].

2.2.3 Phase-Comparison Monopulse

As mentioned previously, the phase-comparison monopulse detection technique is another way to determine the target's angular location. This form of monopulse employs receive beams with different phase centers, which can be obtained, for example, by placing several antennas side-by-side [37]. The angular location is retrieved from evaluating a relative phase difference between the signals received at two phase centers. Note that the signals have the same amplitude. Figure 2.8a illustrates the basic setup of the phase-monopulse method for estimating only one angular coordinate, i.e. either azimuth or elevation, with two antennas in use [41].

The angle of incidence ϕ can be found from the geometrical relations shown in Figure 2.8b between the incoming plane waves and the positions of receiving antennas relative to each other. The two antennas are separated by a distance Δd and the incoming wavefront incidents at the angle ϕ. As demonstrated in the figure, the length difference between the two paths of the incident wavefront results in the phase difference Δa between the incoming signals [42]. From Δa and Δd the angle of incidence can be computed, as seen from the geometrical relations in 2.8b, as

$$\phi = \arcsin(\frac{\lambda \cdot \Delta a}{2\pi \cdot \Delta d}) \tag{2.3}$$

where λ is the wavelength of the signal. If ϕ is equal to 0°, then the target's position coincides with the main antenna axis. This approach requires the exact knowledge of the antenna's phase centers.

2.2.4 Monopulse Beamforming

Handling the signals received from the multiple receive beams for producing the monopulse outputs, i.e. the sum and difference patterns, is generally called monopulse beamforming. In older monopulse radar systems, it is mainly performed in the analog domain. A basic monopulse radar, as schematically presented in this chapter, can, in the analog domain, be realized using passive microwave devices for combining the feed outputs to get the sum and difference patterns [37]. One of the most common microwave devices is a hybrid junction, specifically one type of it which is called a magic-T (or magic-Tee) hybrid junction. Several hybrids in tandem and parallel are needed to generate the output sum and difference beams used for computing the error signal ratio. In the monopulse radar system, such a combination of several hybrids is called a comparator. It is generally placed very close to the feed horns in a compact assembly prior to the receiver unit. Generally, comparators perform the signal combining at a radio frequency (RF). The receiver unit is responsible for converting the RF signals from the monopulse comparator to a form suitable for the monopulse processor, i.e. a radar system's functional block that computes the monopulse ratio. The signals are heterodyned from RF to a baseband or an intermediate frequency (IF) and then converted from analog to digital form through analog-to-digital converters (ADC).

With the advent of advanced ADCs featuring high speed and high dynamic range, monopulse beamforming could also be performed digitally. This can be implemented by simply connecting the terminals of the radar's antenna to four separate ADCs. Newer radars often employ digital beamforming (DBF) in place of the analog monopulse comparator network. A schematic representation of the monopulse system with either analog or digital monopulse comparator network is demonstrated in Figure 2.9.

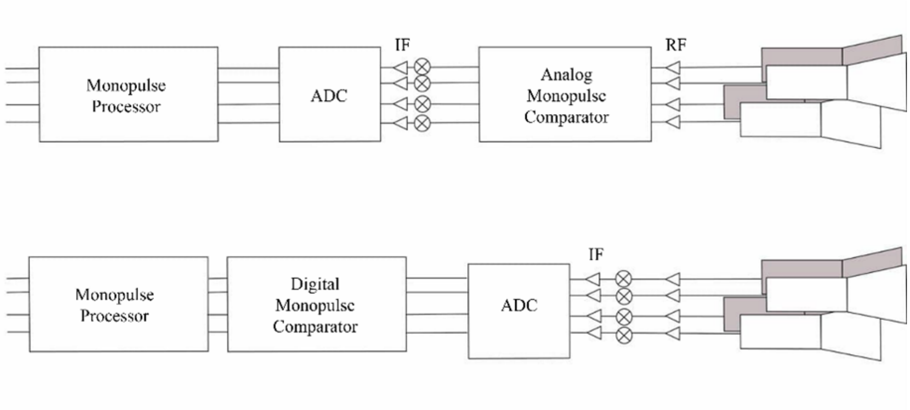

Figure 2.9: Schematic representation of the monopulse radar system with analog and digital comparator networks.

3
Methodology

In Chapter 2, the working principles of the monopulse radar were described. One of the antenna types used in monopulse radars is a parabolic-reflector antenna, in which the mechanical rotation drives the beam steering. However, other types of antennas can also be used. For instance, the monopulse radar can be implemented using phased-array antennas, in which monopulse beamforming is performed digitally, and the beam is usually steered electronically. Phased array antennas have an apparent advantage over reflector or lens antennas, particularly the capability to switch the direction of the beam steering rapidly. This is particularly useful for incorporating the monopulse principles into modern wireless network systems, mainly using phased-array antennas for their operation. This chapter presents a possible solution for integrating the monopulse concept into the BS-IRS-UE model to assist IRS-aided wireless communication.

3.1 Time Division Monopulse Interleaving

This thesis proposes a method of estimating the angular location of the UE relative to the IRS by deploying the monopulse beamforming technique at the BS and the IRS. Currently, there is no proven technical solution for realizing the proposed concept. Nonetheless, it is worth mentioning that the monopulse beamforming is not assumed to be implemented conventionally, i.e. there is no intention to embed a stand-alone monopulse radar system either at the BS or the IRS side. Instead, this thesis suggests exploiting the beamforming capabilities of both the BS and the IRS, which enable the generation of monopulse beam patterns between the BS and the UE. These beam patterns can be realized by performing a convolution on the beams transmitted from the BS towards the IRS and the beams reflected from the IRS's surface in the direction of the UE. Considering the passive nature of the IRS, the monopulse processing or estimation will be handled by the BS. The monopulse sum and difference patterns in azimuth and elevation directions will be formed via the IRS aperture. The procedure implies summing up the IRS's passive reflecting elements into subarrays and applying the weighting, i.e. imposing the phase shifts, at a subarray level. In turn, the BS is responsible for configuring the IRS to set the appropriate weights for creating the sum and difference beam patterns and steering them in the direction of interest. The monopulse estimation of the UE location relative to the IRS is performed using the outputs of the receiver channels (sum and difference beams) formed at the IRS. It is expected that the UE located near the IRS will constantly transmit some data to establish a connection with the closest

BS. The principle of generating the monopulse sum and difference patterns via the IRS is schematically sketched in Figure 3.1.

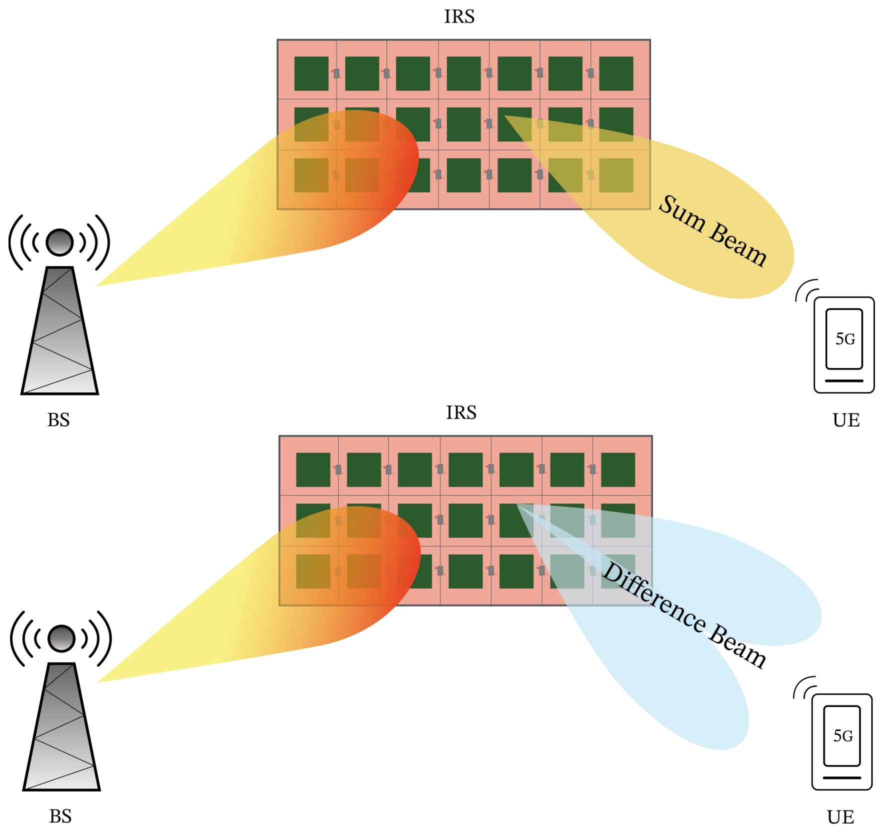

Figure 3.1: The monopulse principle embedded in the BS-IRS-UE setup.

One of the major constraints of the introduced monopulse concept is the loss of the ability to retrieve the angular location of the UE relative to the IRS in a single snapshot, which the monopulse technique is known for. The IRS architecture does not allow the generation of the sum and difference patterns for both azimuth and elevation simultaneously. Therefore, these operations must be done at separate time slots. For instance, in a time slot t_0 the sum beam is created, followed by time slots t_1 and t_2 in which the difference beams are formed for azimuth and elevation estimation. This method is going to be referred to as ***Time Division Monopulse Interleaving (TDMI)***.

3.2 Simulation Tool

This thesis explores the possibility of integrating the monopulse technique into the IRS-aided wireless communication links to estimate the UE's spatial location. For this purpose, an algorithm for evaluating the UE angular information by performing digital monopulse beamforming with subsequent monopulse processing is implemented and tested. For real-world performance evaluation of the proposed TDMI method, it is crucial to test it in the simulation environment, which accurately reflects the real properties of the propagation channel between the BS, the IRS, and the UE. For this purpose, a channel model with incorporated spatial consistency can be used. Spatial consistency reflects the similarity in propagation effects for objects in the propagation environment. For instance, if two UEs are located nearby, they will likely experience the same propagation effects because they are exposed to almost the same scatterers and are at approximately the same distance from the BS [43]. A spatially consistent channel model is a reliable tool for accurately predicting and assessing the impact of the channel on the performance of various techniques in wireless communications, such as massive MIMO precoding or beamforming.

A channel simulator tool called Coffee-Grinder Channel Model (CG) is used to test the aforementioned research objectives. It is designed by Huawei R&D Center in Sweden. GS is a ray-tracing simulator of a spatially consistent wireless channel. CG makes it possible to create complex simulation scenarios based on 3D models of arbitrary 3D environments. One can place signal transmitters and receivers in the predefined 3D environment and evaluate the wireless channel between them. CG is used along with a python-based simulation framework, "cgsim", to evaluate principles of the TDMI technique in the IRS-aided wireless environment.

3.3 Simulation Environment

A 2D top-view perspective of the simulation environment created via CG is shown in Figure 3.2. For demonstration purposes, the IRS and the UE are placed in front of each other on the plane ground with the coordinates (0, 150, 50) and (100, 150, 50), respectively. The coordinates are given in meters. It is assumed that the channel properties between the BS and the IRS are known. Therefore, the BS-IRS link is not considered in the simulation environment. Another assumption is that the IRS and the UE are always located within LOS. Hence, no blockages (e.g., buildings, trees, cars) are added to the modelled environment.

The IRS has a fixed direction of look, i.e. it can not be moved mechanically in any other direction. The placement of the UE relative to the placement of the IRS affects its azimuth and elevation field of view (FoV), i.e. the degree range in which the antenna can scan a horizontal or a vertical plane. With the placement of the IRS and the UE in the 300 m×300 m area as shown in Figure 3.3, the IRS has a limited FoV in azimuth and elevation planes, specifically the sector of ±56° and ±27°, respectively. Any UE placed 100 m apart (x-coordinate) from the IRS and within 0–300 m range in the horizontal plane (y-coordinate) has an azimuth angle in a range bounded by ±56°. In the same way, if the UE is placed 100 m (x-coordinate) from the IRS and within 0–100 m range in the vertical plane (z-coordinate), its elevation angle does not exceed the range of ±27°. However, placing the UE closer to or further from the IRS will impact its azimuth and elevation FoV, i.e. making it narrower or broader due to geometrical properties.

To provide a base for testing the algorithm identifying the UE's angular location, the UE is always located 100 m apart from the IRS in the horizontal plane and 0–100 m in the vertical plane. This is done to maintain a non-changing, static environment

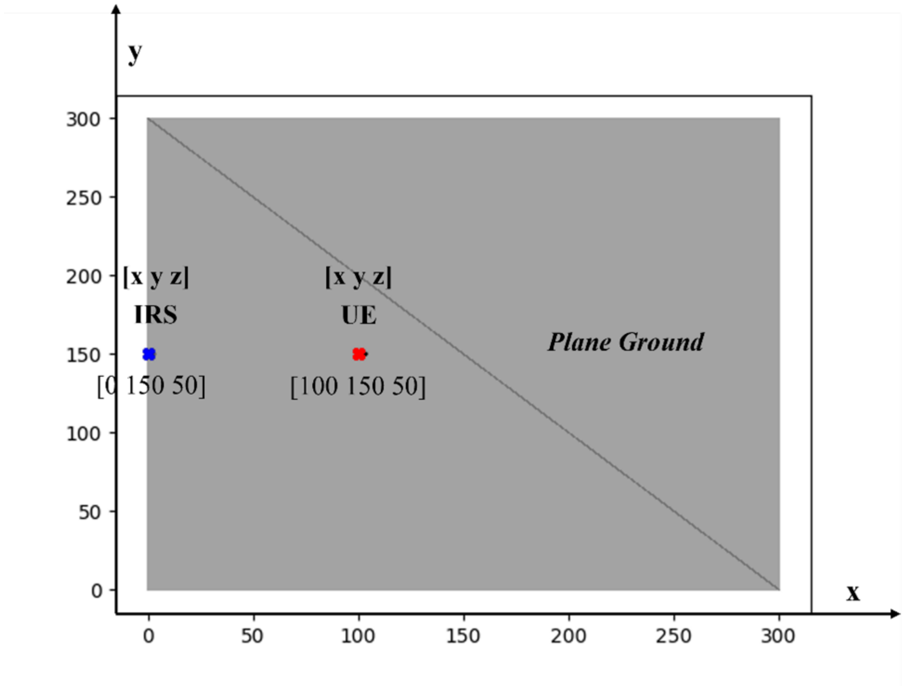

Figure 3.2: A view of the simulation environment in the 2D space.

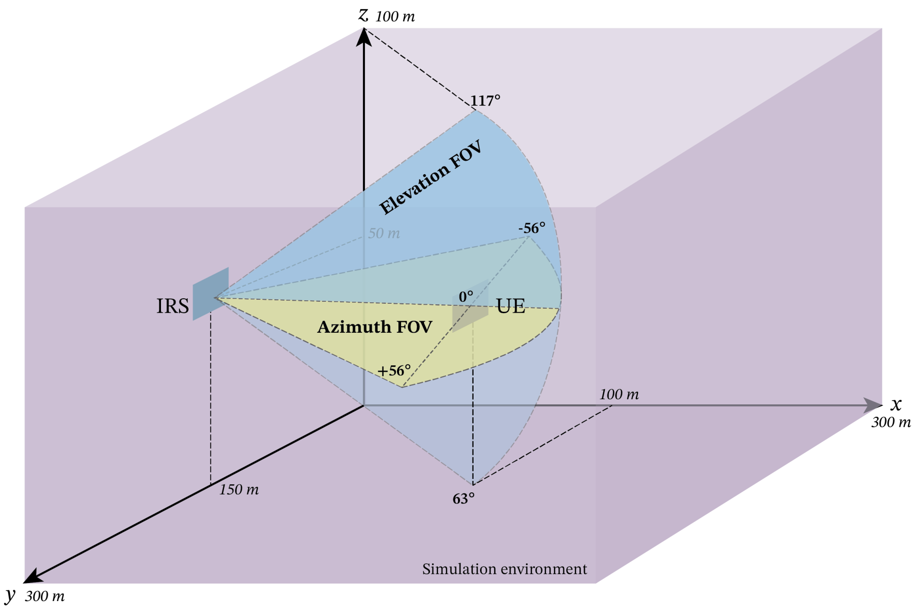

Figure 3.3: A 3D schematic view of the IRS and the UE placement in the simulation environment and the corresponding azimuth and elevation FoV of the IRS.

in which the UE's angular information is bounded to a certain angle range. Figure 3.4 illustrates the UE placement relative to the IRS and the corresponding azimuth and elevation FoV in a 2D perspective.

As previously mentioned, CG provides the possibility for simulating and estimat-

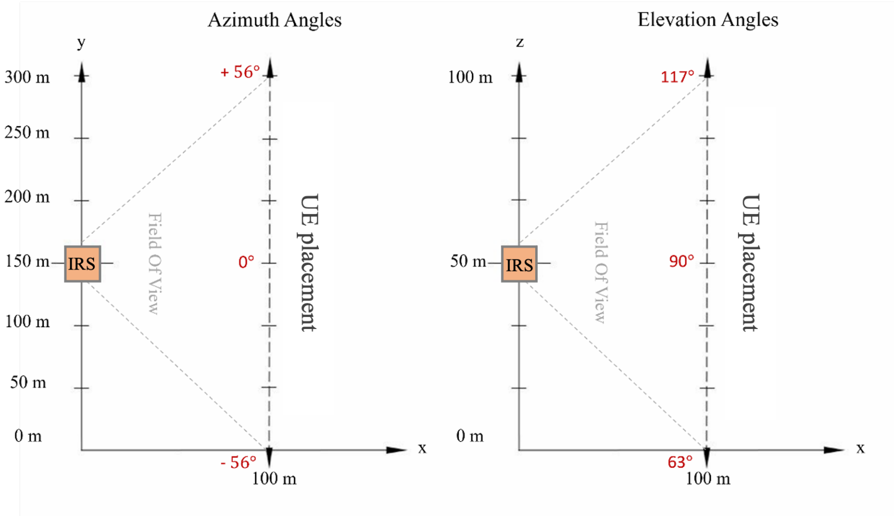

Figure 3.4: A 2D schematic view of the IRS and the UE placement in the simulation environment and the corresponding azimuth and elevation FoV of the IRS.

ing a wireless channel between the IRS and the UE, making it an essential tool for testing the proposed TDMI method. The monopulse estimation is performed on the signal received from the UE. The accuracy of the angular estimation majorly depends on the propagation environment, being a wireless channel which the signal passes through. Numerous non-ideal factors affect the quality of the received signal and the level of SINR, and thus the accuracy of the angle measurement. The non-ideal factors are natural phenomena such as reflection, scattering, and diffraction. The impact of these adverse effects is commonly categorized as path loss, shadowing, and multipath fading. Additionally, the signal will suffer from dispersion in the frequency domain if the UE mobility is present because of the Doppler effect.

This thesis limits itself to the scenario when the horizontal distance between the IRS and the UE is within 10–100 m. Additionally, the distance from the ground plane is kept within 1–100 m for both the IRS and the UE, and it is assumed that no obstructions are placed between them. With respect to the timeline of this research, the focus is on the case when the UE stays stationary. Therefore, the signal distortion caused by the Doppler effect is not a concern of this study. The research has shown that in the presented propagation environment, multipath fading, also known as a small-scale propagation model, is a significant factor causing the degradation of the angular estimation accuracy. This phenomenon occurs because the signal travels along multiple propagation paths between the two endpoints, i.e. a source and a detector. In our scenario, the multipath phenomena are caused by the reflections from the ground plane. The combination of the different versions of the transmitted signal results in amplitude and phase fluctuations and the time delay of the signal received by the UE. In turn, it results in the signal strength varying over a concise period of time. The constructive or destructive interference of the multipath signals explains this. Multipath fading distorts the signal, making it harder to accurately evaluate the source (e.g. the UE) angular location using the monopulse technique.

The multipath between the IRS and the UE is schematically illustrated in Figure 3.5a, and multipath fading is represented in 3.5b.

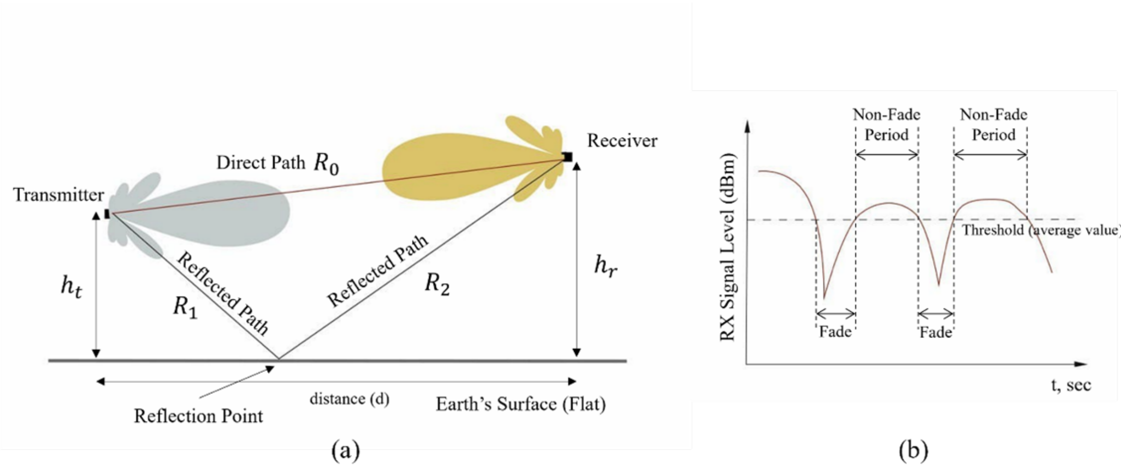

Figure 3.5: The multipath between the IRS and the UE (a); Representation of the multipath fading (b).

Tools integrated into the CG's functionality enable simulating the aforementioned propagation mechanisms. It is vital to conduct tests in a non-ideal environment to estimate the performance and reliability of the monopulse technique embedded into the BS-IRS-UE setup in real-life conditions. The simulation environment in the 3D space is presented in Figure 3.6. Figure 3.6a shows an example of a wireless channel between the IRS and the UE, in which the signal propagates according to the multipath mechanism caused by the presence of reflections and scattering. Blue lines represent multiple reflection paths, whereas the red line is a direct path. Hereafter, this type of wireless channel will be referred to as a non-ideal channel. Figure 3.6b shows a wireless channel with a single direct path between the IRS and the UE, also called a LOS path. This is the free space or direct propagation model. It is an idealized model of the propagation environment, which has an important application. This model predicts the received signal strength if the IRS and the UE have a clear, unobstructed LOS path between them when neither absorbing obstacles nor reflecting surfaces are considered. Henceforth, this type of wireless channel will be referred to as an ideal channel. In terms of this research, it is crucial to have access to the idealized propagation model as it serves as a base reference for understanding the properties of the monopulse technique integrated into the BS-IRS-UE setup.

3.4 Choice of Monopulse Detection Technique

This thesis adopts an amplitude-comparison monopulse detection technique as the primary approach for estimating the DoA or angular information of the target, which is the UE. The main reason for that is the limitations related to the physical construction of the IRS. A phase comparison monopulse detection technique is based

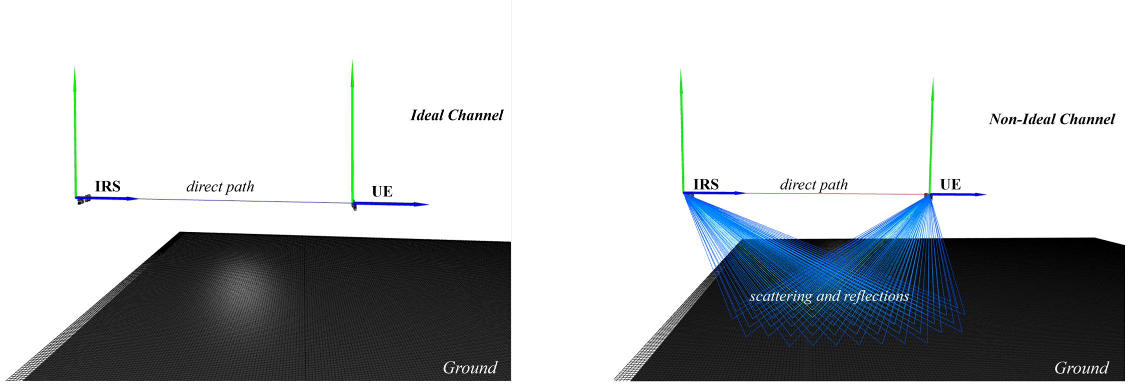

(a) The ideal channel. **(b)** The non-ideal channel.

Figure 3.6: A view of the simulation environment in the 3D space.

on calculating the phase difference of the signals received from the source. In a parabolic-reflector or an active phased array antenna, the phase difference can be extracted directly from the neighbouring antennas or the antenna elements placed at different phase centers. In the BS-IRS-UE setup, the signal from the UE is initially impinging on the IRS's surface. Therefore, the phase difference can be retrieved from two adjacent IRS elements sensing the incident wave. However, the IRS being a planar surface composed of passive reflecting elements with no embedded receiver chains, makes it unfeasible to exploit the phase-comparison method. It is impossible to detect the signal at each particular element as it has no connection to the receiver unit and to estimate the phase difference. To sum up, due to the passive nature of the IRS, it is hard for the BS to get an accurate phase calibration between itself and the surface. In turn, the amplitude-comparison detection technique operates on the amplitude difference of the received signals, which is easier to evaluate at the BS.

3.5 Monopulse Subarrays

An essential step in this research is to deploy and test the monopulse beamforming and processing digitally via CG. The implementation is done in several stages. First, monopulse beamforming is explored. It is a technique applied on the antenna level to form sum and difference monopulse patterns. As noted in Chapter 2, monopulse beamforming can be performed in an analog circuitry by a tandem of the reflector antenna fed by, e.g. two or four feed horns and a comparator network. Another way is to perform it digitally after converting analog signals into an equivalent digital binary code by ADCs. Digital implementation has become preferable with the advent and advancement of phased-array antennas. Most modern monopulse radars adapt the classical monopulse techniques to array antennas [44]. Due to the large number of elements constituting the phased array antenna, operation at the element level is impractical. Thus, for implementing the monopulse technique, the aperture of the phased array antenna can be split into symmetrical quadrants by partitioning the array elements into subarrays. In the initialization stage, separate excitations, with different phase shifts, are applied to each antenna element to achieve beam steering in the desired direction. Afterwards, additional weighting at the subarray level is applied to generate the monopulse sum and difference patterns. An example of a phased array antenna comprising N×M elements, which are subdivided into quadrants, is presented in Figure 3.7.

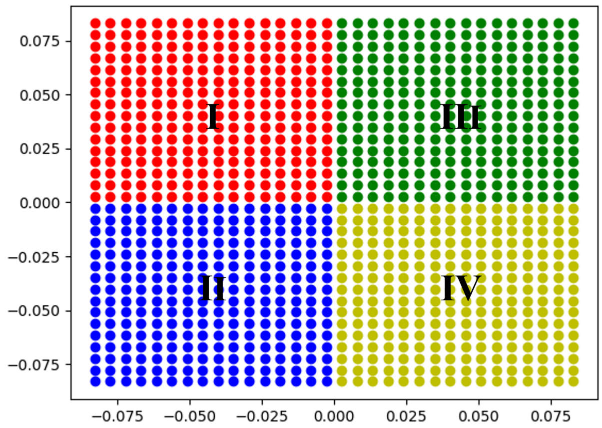

Figure 3.7: Monopulse subarrays.

The IRS differs in its nature and functionality from an active phased array antenna. Nonetheless, the IRS is a planar surface consisting of rows and columns of passive reflective elements, which can also be subdivided into quadrants. The BS controls the phase shift excitation of the IRS's elements. Therefore, the monopulse beamforming can be performed via the IRS's aperture. The monopulse processing is done only with the digitalized subarray outputs. With respect to the arrangement of the four subarrays in Figure 3.7, the monopulse sum and difference patterns are formed according to (2.1), where I, II, III, and IV are denoted as A, B, C, and D. A monopulse ratio, also called an error signal, is calculated according to (2.2).

CG toolbox does not yet have a prototype of IRS that could be used for testing. Hence, the IRS is replaced with a planar phased array for implementing and verifying an algorithm for identifying the UE angular location. In the simulation environment shown in Figure 3.3, a phased array serves as the IRS, and an omnidirectional antenna represents the UE.

3.6 Multi-Step Monopulse Angle Estimation Algorithm

A feasible and efficient algorithm is developed for estimating azimuth and elevation angle components of the UE relative to the IRS by applying monopulse beamforming and monopulse amplitude-comparison detection techniques. The algorithm consists of two functional blocks, and it is called a **multi-step monopulse angle estima-**

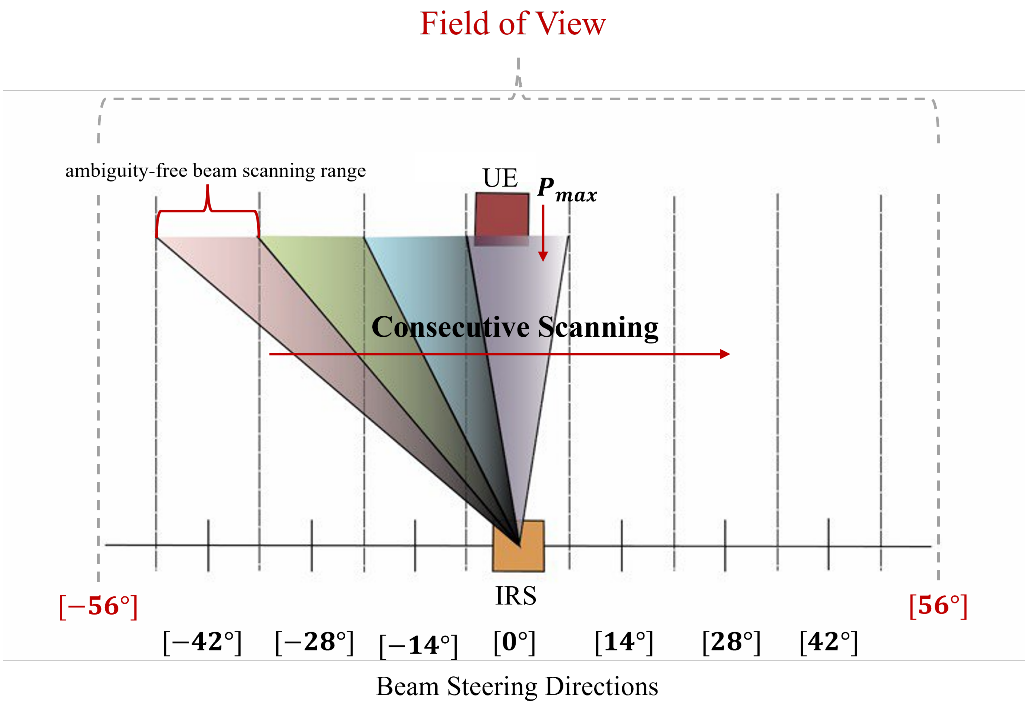

Figure 3.8: The multi-step monopulse detection algorithm: coarse detection of the UE location.

tion algorithm.

Initially, from the BS-IRS perspective, the UE's location is completely unknown. It is only assumed that the UE is located within the IRS's FoV. Due to the narrowness of the monopulse radiation pattern formed via the planar phased array, it is impossible to determine the precise angular location of the UE within the observation area with one monopulse snapshot. Therefore, a coarse detection of the UE's direction over the IRS's FoV is first carried out. This step precedes the monopulse amplitude processing procedure, during which an accurate estimation of the UE's azimuth and elevation angular components is done. The IRS's FoV is scanned with the subsequent monopulse sum and difference patterns, as seen in Figure 3.1), according to the pre-calculated codebook, i.e. along the grid of steering directions. The power of the received signals at each steering direction is measured, and then the values are compared. The direction with the maximum gain is considered to be the preliminary UE's DoA. As such, during the first step, which can also be referred to as a search mode, the IRS's steering direction is determined. The subsequent monopulse processing is carried out within the angle range of the defined steering direction. The coarse detection of the UE's location is illustrated in Figure 3.8.

Steering directions are predefined for the planar array based on its configuration, defined by the array's number of elements. This thesis considers a planar, linear, and equispaced phased array with the subelement spacing, d_y, between N elements in each column and, d_x, between M elements in each row, equal to 0.5λ. By adjusting the phase shifts for each element, the array's pattern can be steered along the x-axis and y-axis. Therefore, a 2D angular scan can be carried out in both horizontal and vertical planes. The width of the radiation beam pattern is inversely proportional to the size of the planar array. The larger the planar array size is, i.e. the more elements it comprises, the narrower a beamwidth can be acquired. Correspondingly, the width of the monopulse sum and difference patterns depends on the size of the planar array via which they are formed. The width of the monopulse patterns affects the *ambiguity-free* beam scanning range, that is, an angle range within which a single monopulse snapshot can make a unique DoA estimation. In the monopulse radar system, ambiguity can occur when an interfering signal coming from outside the antenna's FOV is interpreted to come from inside its FOV. This can e.g. be a signal that enters the receiver via a sidelobe, and it leads to a false estimation of the DoA. Thus, unwanted ambiguities lead to a false estimation of DoA, i.e. azimuth and elevation angles of the target [45]. In the example demonstrated in Figure 3.8, the IRS's FoV, covering angle range $[-56°, +56°]$ in the azimuth plane, is scanned by the monopulse sum and difference patterns with an ambiguity-free scanning range of 14°. These monopulse patterns are formed via a planar array of size 32×32. The number of beam steering directions can be obtained through the following formula

$$k_{az} = \left\lceil \frac{\Phi}{\Theta_{az}} \right\rceil - 1 \tag{3.1a}$$

$$k_{el} = \left\lceil \frac{\Phi}{\Theta_{el}} \right\rceil - 1 \tag{3.1b}$$

where k_{az} and k_{el} are numbers of steering directions in azimuth and elevation planes, Φ is the IRS's FoV, Θ_{az} and Θ_{el} are azimuth and elevation ambiguity-free beam scanning ranges. The steering step numerically equals the ambiguity-free beam scanning range value. The stepping starts from the azimuth boresight direction 0° and the elevation boresight direction 90°. As such, for the example presented in Figure 3.8, seven beam steering directions, $k_{az} = [-42°, -28° - 14°, 0°, +14°, +28°, +42°]$, are defined.

After detecting the UE in a search mode, there follows an angle estimation by applying the monopulse amplitude-comparison detection technique, which is presented in Figure 3.9. This procedure may be performed with the same received data snapshot used for the detection, as it is only an additional processing step. The data is retrieved through the subsequent excitation of the monopulse sum and difference patterns towards the direction of the UE. Azimuth and elevation monopulse ratios are calculated for the defined steering direction, and their values are saved. As a conventional monopulse radar system is not used in this thesis, the azimuth and elevation angles are computed from the monopulse ratio measurements in a novel way. The angles are estimated according to the known mapping between the monopulse ratio and azimuth or elevation angles. This mapping is retrieved while simulating the ideal wireless propagation channel between the IRS and the UE. For each azimuth and elevation angle in an angle range corresponding to each steering direction, a monopulse ratio is calculated and stored in an array. Therefore, each azimuth and elevation angle in the IRS's FoV is mapped to the monopulse ratio value retrieved under the conditions of the ideal channel. Afterwards, an algorithm is implemented for determining the closest value of the ideal monopulse ratio measurements to one obtained in a real-life detection process. Then this value is mapped to the azimuth or the elevation angle. Thus, the angle estimation is accomplished.

To accurately estimate the UE angle coordinates, it is vital to acquire accurate measurements of the monopulse ratio in the non-ideal channel, which are numerically close to the ones extracted in the ideal channel.

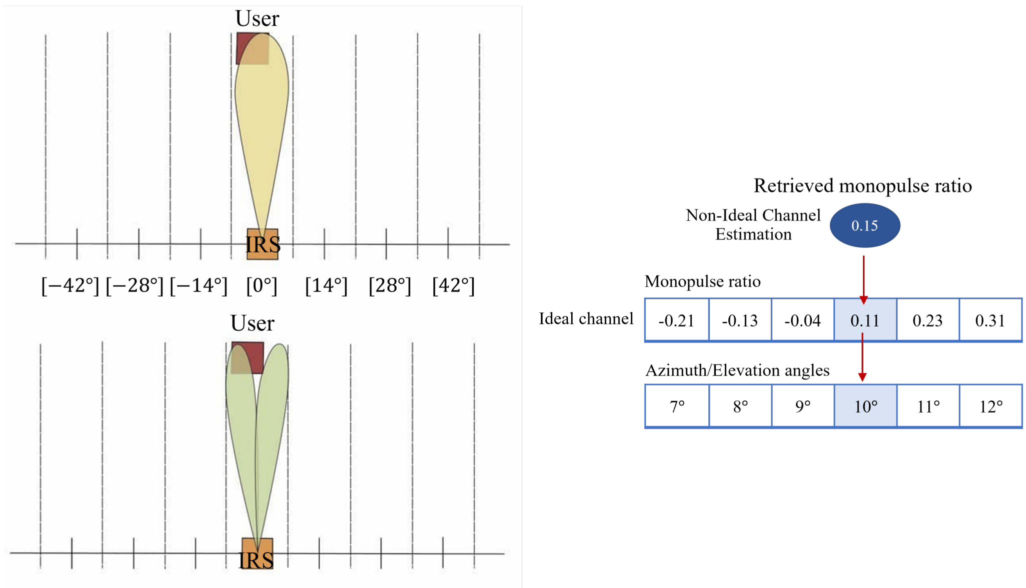

Figure 3.9: The multi-step monopulse detection algorithm: accurate estimation of the UE angular location.

4

Results and Discussion

This chapter outlines the results obtained from applying the introduced TDMI concept for estimating UE's azimuth and elevation angular coordinates in the IRS-aided communication link.

4.1 Monopulse Error Signal Simulation in Ideal and Non-ideal Channels

As mentioned in Chapter 3, due to the limitations of the simulation framework used in this thesis, IRS is replaced with a planar phased array for testing the proposed TDMI method. Several array configurations are examined: 16×16, 32×32, 46×46, 64×64. An array configuration denotes an array comprising N×M elements. Applying the monopulse technique with phased arrays of smaller sizes did not demonstrate decent accuracy in estimating the UE's angular information. The suggested array configurations are chosen randomly but with the consideration of the potential IRS size. These array configurations are tested with the multi-step monopulse angle estimation algorithm, and the estimation accuracy for each configuration is evaluated.

4.1.1 Array Configuration: 16×16

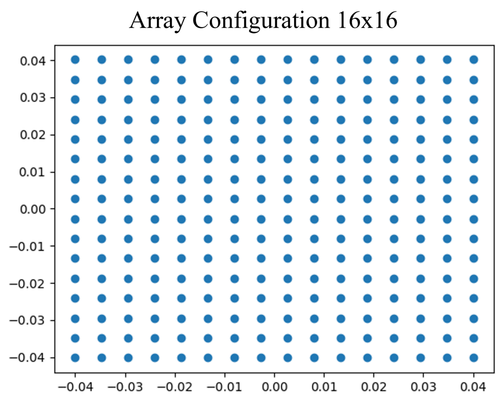

Figure 4.1: A planar phased array of size 16×16.

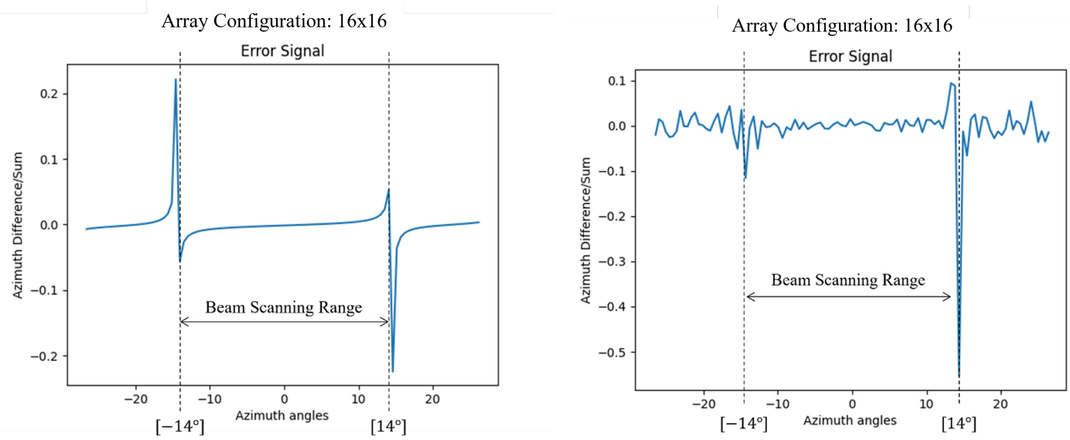

(a) Error signal obtained in the ideal channel.

(b) Error signal obtained in the non-ideal channel.

Figure 4.2: Error signal obtained for the array configuration 16×16.

At first, a planar array of size 16×16 is chosen for testing the proposed multi-step monopulse angle estimation algorithm. A simulation environment with the IRS and the UE placement, as demonstrated in Figure 3.3, is considered. IRS's FoV is fixed and limited to the angle range $[-56°, +56°]$ in the azimuth plane and $[63°, 117°]$ in the elevation plane.

Figure 4.1 schematically shows the displacement of 256 antenna elements on the square-shaped planar surface. The subelement spacing is 0.5λ. Figure 4.2a shows an error signal computed by the formula (2.2) for this array configuration. The antenna's boresight is at 0°. The monopulse beam scanning range is 28°. It can be observed from the plot that the error signal's curve has a steadily increasing linear region within a certain range and reaches two of its peaks at $-14°$ and $+14°$. These peaks denote the beginning and the end of the ambiguity-free beam scanning range. The monopulse ratio is used to determine the direction of the target in terms of azimuth and elevation angles. Therefore, for an accurate estimation, it is crucial to verify that the curve of the monopulse ratio keeps the described shape, thus showing that the monopulse detection is performed accurately.

Suppose the UE is located within the ambiguity-free beam scanning range, which is $[-14°, +14°]$ in the illustrated example. In this case, its angular location can be obtained with good accuracy by the monopulse technique. However, suppose the UE's azimuth angle is outside the specified range of azimuth angles, and the antenna's boresight axis points at 0°. In that case, the angular information can not be derived due to the presence of ambiguity. For estimating the azimuth angle of the UE located outside the $[-14°, +14°]$ range, the antenna's monopulse beams should be steered towards the direction of the UE. Suppose the IRS's FoV covers angle range $[-56°, +56°]$ in the azimuth plane as shown in Figure 3.3, and the UE's true azimuth angle is 31°. According to (3.1) three steering directions for the array configuration 16×16 can be defined, specifically $[-28°, 0°, +28°]$. Therefore, to accurately estimate UE's

DoA in terms of azimuth angle, the boresight of the sum and difference patterns should be steered at 28° so that the antenna's ambiguity-free beam scanning range covers the desired angle, and the monopulse estimation algorithm can be applied. The same constraints are valid for estimating the UE's elevation angle.

The error signal presented in Figure 4.2a is retrieved by the monopulse amplitude-comparison technique under the conditions of the ideal channel. This kind of propagation channel is not affected by any reflection, scattering, or diffraction present in a natural environment. Therefore, the simulation results can be considered an ideal model of the monopulse technique utilized in the BS-IRS-UE setup, which can be used as a reference.

The amplitude-comparison monopulse with the same array configuration (16×16 elements) is also tested under the conditions of the non-ideal channel. It is discovered that, in this case, the monopulse technique applied with the specified array size does not provide satisfactory results. Figure 4.2b shows the error signal obtained in the non-ideal channel. It can be noticed that it fluctuates significantly over the beam scanning range, and its curve does not preserve linearity. This error signal can not be used for determining the UE's DoA as it will significantly lower the estimation accuracy. This phenomenon occurs due to the adverse effects of the non-ideal channel, mainly due to scattering and reflections causing the multipath fading. The monopulse sum and difference patterns formed via the array of size 16×16 pick up the undesired multi-paths of the signal transmitted by the UE, which interfere with each other and distort the received signal. Consequently, it impacts the derivation of the monopulse ratio, whose value is unreliable for further estimation. A possible solution is to make the width of the monopulse patterns sufficiently small and precisely directed toward the UE to avoid multipath effects.

As it was previously discussed, one of the ways of narrowing the width of the monopulse patterns is by increasing the size of the planar array. Therefore, several arrays of bigger size are tested (32×32, 46×46, 64×64), and their performance is evaluated.

4.1.2 Array Configuration: 32×32

The ambiguity-free beam scanning range of the array configuration 32×32 is 14°. Considering the initial array's boresight is directed at 0°, the monopulse beam patterns should be steered horizontally and vertically along the IRS's FoV according to the predefined beam steering directions. The number of steering directions is calculated by the formula (3.1). The steering step is 14°. Figure 4.3 illustrates the error signal obtained for each of the steering directions in both azimuth and elevation planes. The blue curve represents the error signal obtained in the ideal channel, whereas the red curve is the error signal obtained in the non-ideal channel.

In the case of azimuth angles (Figure 4.3a), it can be seen that the red curve almost precisely overlaps the shape of the blue, meaning the values of the non-ideal error

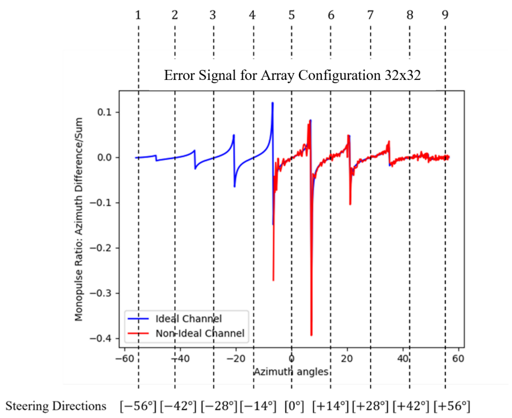

(a) Error signal obtained for each of the steering directions in the azimuth plane.

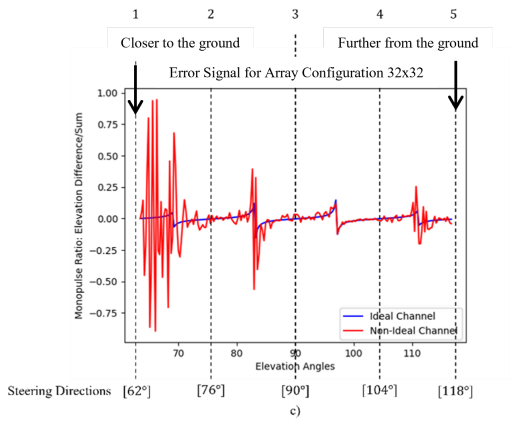

(b) Error signal obtained for each of the steering directions in the elevation plane.

Figure 4.3: Error signal obtained for each of the steering directions in azimuth and elevation planes for the array configuration 32×32.

signal are very close to the ideal ones. Nevertheless, the red curve still fluctuates noticeably, primarily when the array points at ±42° and ±56° steering directions. In general, it can be explained by noting that the monopulse beam patterns formed via the array of the size 32×32 are not narrow enough to filter out all the undesired reflected or scattered signals destructing the LOS signal.
For the elevation angles (Figure 4.3b), it can be observed that the non-ideal error signal significantly oscillates at 62° and 76° steering directions. These angles correspond to the UE being placed close to the ground (see Figures 3.3 and 3.4). Several factors can explain this phenomenon.

First, due to the nature of the digital beam steering, the beam patterns get wider when steered to the left or right from 0°. Therefore, the monopulse sum and difference patterns gather extra noise, and the derivation of the monopulse ratio gets more erroneous. Thus, the estimation accuracy is affected. Figure 4.4 shows a 2D view of the monopulse sum and difference patterns steered to 0° and −56°. It is visible that both sum and difference patterns become wider when their direction is changed towards the extreme steering angle values.

Secondly, apart from the monopulse beams getting wider when steered digitally up or down from 90°, if the UE is located closer to the ground, more scattered and reflected signals pass through the monopulse patterns in comparison to the UE being placed in front of the array whose elevation boresight is steered to 90°. These signals become a source of interference which disrupts the LOS signal. Hence, the calculation of the monopulse ratio is carried out inaccurately. Figure 4.5 visualizes the described phenomenon.

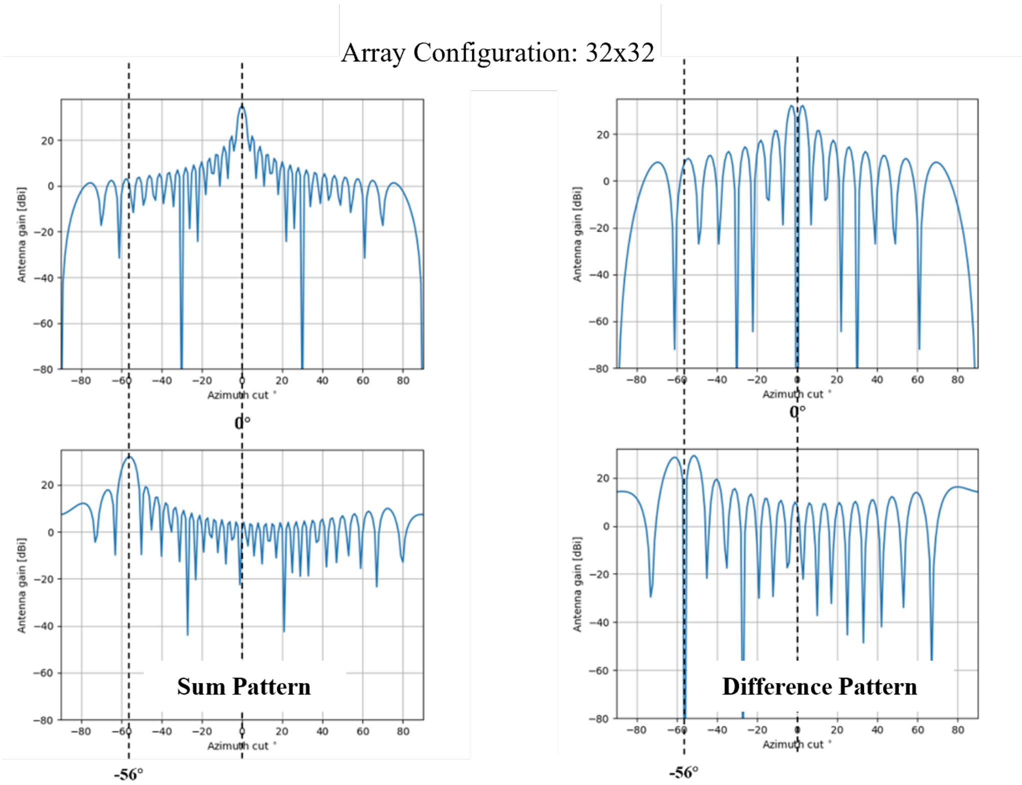

Figure 4.4: A 2D view of the monopulse sum and difference patterns for the array configuration 32×32.

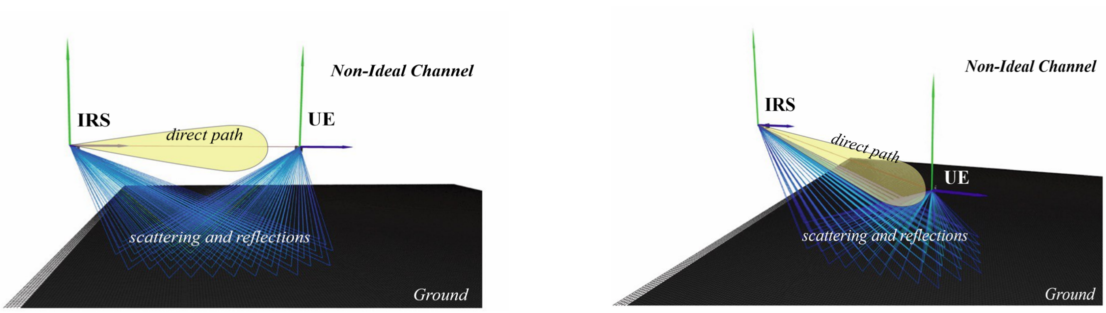

(a) The direction of a phased array radiation pattern when the IRS and the UE are placed in front of each other high above the ground.

(b) The direction of a phased array radiation pattern when the UE is placed closer to the ground relative to the IRS.

Figure 4.5: An illustration of a phased array radiation pattern in the non-ideal channel with the multipath signal propagation.

Figure 4.6 illustrates a 3D model of the monopulse sum and difference beam patterns steered to 0° (Figure 4.6a) and −56° (Figure 4.6b), respectively. It can be seen that when the patterns are steered to the edge of the scanning grid, not only do their main lobes become noticeably wider, but also the side lobes. The broadening of the side lobes facilitates the side effects of the digital steering, i.e. more undesirable external noise is being captured, adversely affecting the monopulse technique's estimation capability.

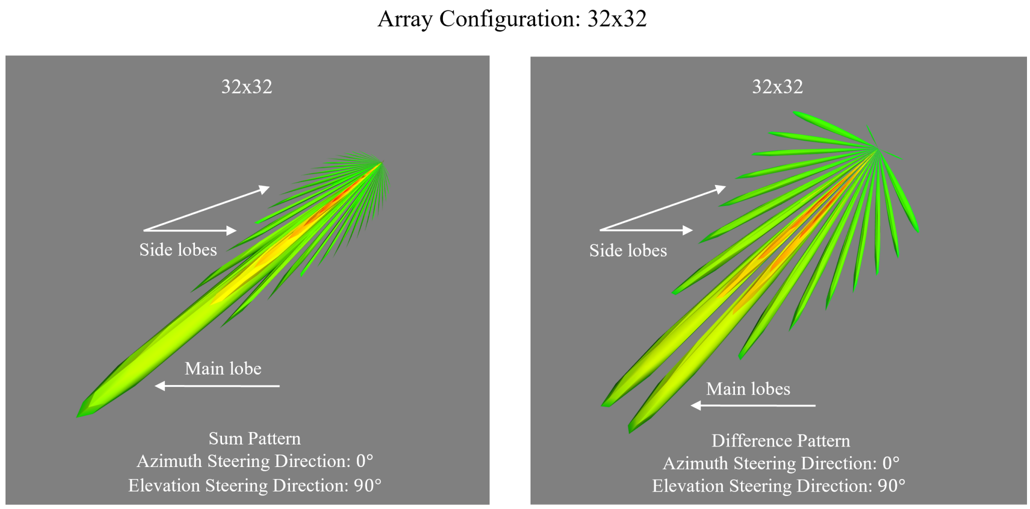

(a) The monopulse sum and difference patterns steered to 0° in the azimuth axis.

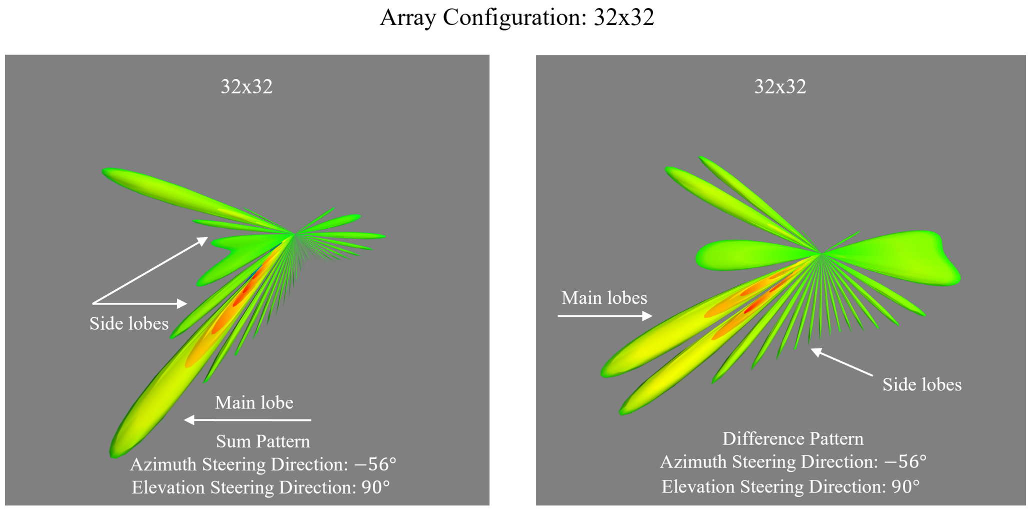

(b) The monopulse sum and difference patterns steered to −56° in the azimuth axis.

Figure 4.6: A 3D view of the monopulse sum and difference patterns for the array configuration 32x32.

4.1.3 Array Configurations: 46×46 and 64×64

The main principles and characteristics of the monopulse beamforming and beam steering described in the previous subsection are relevant when utilizing arrays of larger sizes, like 46×46 and 64×64. Figure 4.7 shows the error signal for each of the azimuth and elevation steering directions for the array configuration 46×46, consisting of 2116 elements. As the array size increased, the monopulse sum and difference patterns got narrower, and the ambiguity-free beam scanning range decreased to

10°. Therefore, the azimuth and elevation planes are chunked into more steering directions. The non-ideal error signal oscillates considerably less, following the shape of the ideal error signal more precisely. However, some trends remain unchanged when increasing the array dimensions, namely the monopulse ratio obtained when steering in the azimuth angles ±50°, ±40°, and elevation angles 60°, 70°. This can be explained by the same physical phenomena described in the previous subsection.

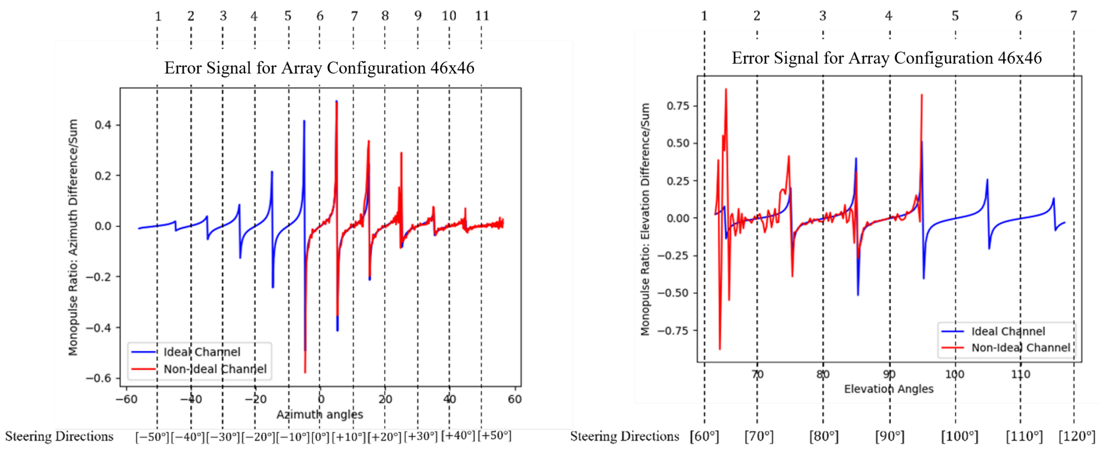

Figure 4.7: Error signal obtained for each of the steering directions in azimuth and elevation planes for the array configuration 46×46.

Figure 4.8 plots the error signal for each of the azimuth and elevation steering directions for the array configuration 64×64, consisting of 4096 elements. The monopulse sum and difference patterns got narrower again, and the ambiguity-free beam scanning range decreased to 6°. Consequently, the number of steering directions increased. The antenna radiation pattern resembles the shape of a pencil and, therefore, is called a pencil beam.

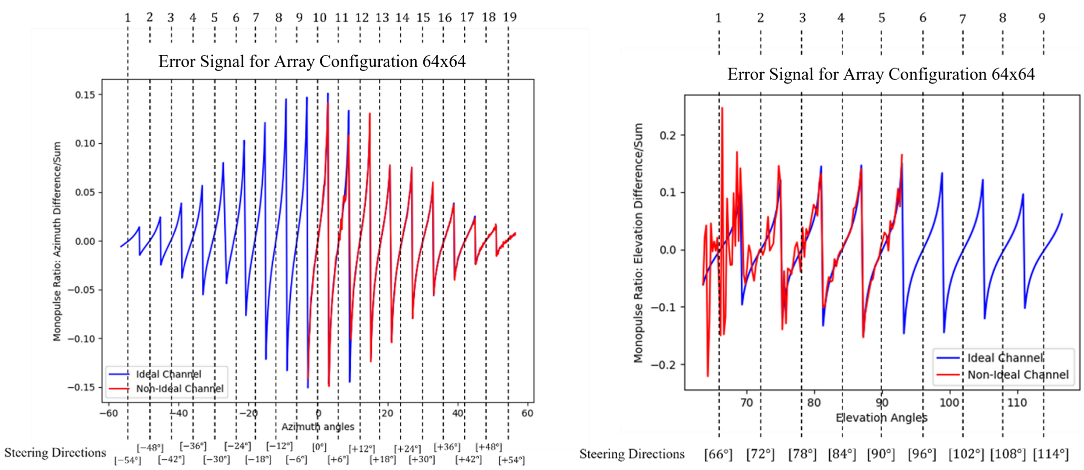

Figure 4.8: Error signal obtained for each of the steering directions in azimuth and elevation planes for the array configuration 64×64.

For this array configuration, the curve of the non-ideal error signal obtained for azimuth angles is almost identical to the ideal one, meaning the values of the monopulse ratio retrieved in the non-ideal channel are very close to the ones calculated under the ideal conditions. The non-ideal monopulse ratio is still noticeably erroneous for elevation angles, but in general, the multipath fading that causes this issue is primarily of concern in elevation tracking. Thus, lower estimation precision in numerical results is expected.

The 2D and 3D views of the monopulse sum and difference patterns for array configurations 46×46 and 64×64 are attached to Appendix A.

4.2 Monopulse Angle Estimation for UE Localization

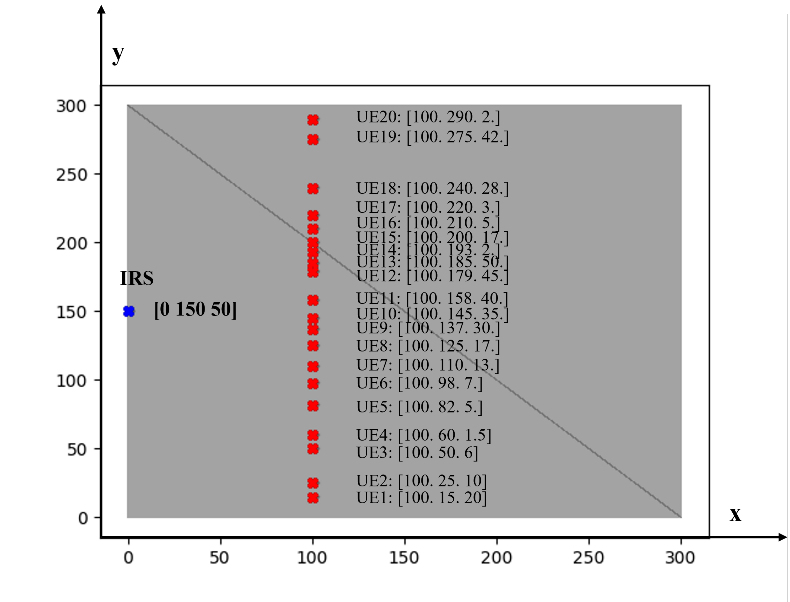

Figure 4.9: Simulation test: arbitrary placement of 20 UE in the simulation environment.

For testing the multi-step monopulse angle estimation algorithm proposed in this thesis, 20 UEs are arbitrarily placed in the simulation environment, as demonstrated in Figure 4.9. Their azimuth and elevation angles are evaluated using three array configurations: 32×32, 46×46, 64×64. The results of the angle estimation for each array configuration are attached to Appendix B. The measurements of the UE's azimuth and elevation angle coordinates obtained in the ideal channel are referred to as true direction, and the estimated angles obtained under the non-ideal channel conditions are referred to as estimated direction. The estimation error, i.e. the deviation between the true and estimated angle values, is calculated for each UE. Table 4.1 summarizes the test results.

As the array size increases and monopulse sum and difference patterns become narrower, the accuracy of the detection of the UE's location grows, and the average angle error decreases. The explanation of the observed correlation is given in the previous subsections, i.e. the narrower the beam patterns are used, the better they filter out the undesired scattered and reflected signals paths that attenuate the LOS signal. Therefore, obtaining more accurate measurements of the monopulse ratio is possible even when multipath fading obstructs the wireless propagation channel. Numerical results reflect that the monopulse processing is feasible when applying each array configuration. However, it is seen (Table 4.1) that usage of the array consisting of 64x64 elements provides the best performance in terms of angle estimation, confirmed by the low estimation error of 1.588° and 1.538° for azimuth and elevation angles, respectively.

Array configuration	**32x32**	**46x46**	**64x64**
Beam Scanning Range	14°	10°	6°
Average Azimuth Angle Deviation	6.117°	4.334°	1.588°
Average Elevation Angle Deviation	4.698°	2.835°	1.538°

Table 4.1: The average azimuth and elevation angle error calculated for the three array configurations: 32×32, 46×46, 64×64.

5
Conclusion

This thesis explored a novel solution for estimating the channel between the BS, the IRS, and the UE. A TDMI concept, based on the well-known amplitude-comparison monopulse technique exploited in tracking systems, was introduced as a new approach for spatial channel estimation in IRS-aided communication links between BSs and UEs. It is proposed to jointly exploit the BS and the IRS beamforming capabilities for deploying digital monopulse beamforming at the IRS site. The multi-step monopulse angle estimation algorithm was developed for acquiring the angular location of the UE in terms of azimuth and elevation angular coordinates. The algorithm's performance was tested and numerically evaluated. It is shown that the proposed method can be used to localize the UE accurately. An estimation accuracy for elevation and azimuth angles was about 4.7° and 6.1° when using 32×32 IRS configuration. For 46×46 and 64×64 IRS configurations, estimation accuracies were 2.8°, 4.3° and 1.5°, 1.6° for elevation and azimuth angles, respectively. As such, the highest estimation accuracy was achieved by exploiting the IRS comprising the largest number of scattering elements.

Based on the simulation results presented in this thesis work, it can be concluded that the proposed TDMI concept can be potentially integrated into IRS-aided wireless systems. However, a significant enhancement of the currently presented solution is needed. For modern wireless communications, it is vital to support high-mobility multi-user scenarios, which are not explored throughout this research.

6
Future Work

Future work concerns a deeper dive into the prospects of applying the monopulse technique in the BS-IRS-UE setup for estimating a spatial channel between the BS, the IRS, and the UE. The research work done in this thesis shows that the monopulse processing provides an accurate estimation of the UE's angular location if a considerably large IRS is used and strictly LOS propagation is considered. However, this thesis considers a significantly simplified use case. First of all, only the static nature of the UE is considered. Besides, the capability to determine the DoA only of a single UE per unit of time is verified. The proposed TDMI concept's future development should focus on exploring the multi-user high-mobility scenarios.

Nonetheless, a few approaches already introduced in this thesis could be potentially enhanced. The first main modification that could be made is to the multi-step monopulse angle estimation algorithm. The presented algorithm has shown robustness and effectiveness in addressing the given task of acquiring the UE's azimuth and elevation angular coordinates relative to the IRS. However, it can become noticeably time-consuming if the IRS grows in size to achieve narrower monopulse sum and difference patterns, increasing the number of steering directions. The coarse detection of the UE's location becomes redundant as it is conducted via a sequential scan of the observed area in a grid of steering directions. Instead, the hierarchical search can be introduced. The concept implies switching from wider beams to narrower ones while scanning the IRS's FoV to determine the UE's approximate direction. This approach reduces the number of steering directions. Hence, the number of iterations needed to find a coarse UE's DoA decreases. However, it is still unknown to which extent the monopulse beam patterns can be broadened via the IRS aperture, leaving another challenge for future research.

The second main modification that could be considered is the replacement of the omnidirectional antenna at the UE's side with a high-gain directional antenna. It is another way of improving the angle estimation accuracy without steadily enlarging the number of the IRS's passive scattering elements. A directional antenna at the UE's side will provide a LOS propagation of the signal between the IRS and the UE, not affected by ground scatterings and reflections. This approach might require a smaller IRS configuration to achieve the desired estimation accuracy. Therefore, this solution might be more cost-effective. However, additional signal processing is required on the UE's side, as its radiation pattern should also be directed toward the IRS.

Bibliography

[1] Yuanwei Liu et al. "Reconfigurable Intelligent Surfaces: Principles and Opportunities". In: *IEEE Communications Surveys Tutorials* (2021), pp. 1–1. DOI: 10.1109/COMST.2021.3077737.

[2] Mohamed A. ElMossallamy et al. "Reconfigurable Intelligent Surfaces for Wireless Communications: Principles, Challenges, and Opportunities". In: *IEEE Transactions on Cognitive Communications and Networking* 6.3 (2020), pp. 990–1002. DOI: 10.1109/TCCN.2020.2992604.

[3] Jing Zhang et al. "5G Millimeter-Wave Antenna Array: Design and Challenges". In: *IEEE Wireless Communications* 24.2 (2017), pp. 106–112. DOI: 10.1109/MWC.2016.1400374RP.

[4] Xiaohu Ge et al. "5G Ultra-Dense Cellular Networks". In: *IEEE Wireless Communications* 23.1 (2016), pp. 72–79. DOI: 10.1109/MWC.2016.7422408.

[5] Qingqing Wu et al. "Intelligent Reflecting Surface Aided Wireless Communications: A Tutorial". In: *CoRR* abs/2007.02759 (2020). arXiv: 2007.02759. URL: https://arxiv.org/abs/2007.02759.

[6] Qianqian Du et al. "Uplink Channel Estimation for Intelligent Reflecting Surface Aided Direct and Reflected Users". In: (2022), pp. 1–6. DOI: 10.1109/VTC2022-Spring54318.2022.9860583.

[7] Chen Dongxu. *5G power: Creating a green grid that slashes costs, emissions & energy use*. July 2020. URL: https://www.huawei.com/us/huaweitech/publication/89/5g-power-green-grid-slashes-costs-emissions-energy-use.

[8] Özgecan Özdogan, Emil Björnson, and Erik Larsson. "Intelligent Reflecting Surfaces: Physics, Propagation, and Pathloss Modeling". In: *IEEE Wireless Communications Letters* PP (Dec. 2019), pp. 1–1. DOI: 10.1109/LWC.2019.2960779.

[9] Ana Dıéaz-Rubio et al. "From the generalized reflection law to the realization of perfect anomalous reflectors". In: *Science advances* 3.8 (2017), e1602714.

[10] Shaoqing Zhou et al. "Spectral and Energy Efficiency of IRS-Assisted MISO Communication With Hardware Impairments". In: *IEEE Wireless Communications Letters* 9.9 (2020), pp. 1366–1369. DOI: 10.1109/LWC.2020.2990431.

[11] Shimin Gong et al. "Toward Smart Wireless Communications via Intelligent Reflecting Surfaces: A Contemporary Survey". In: *IEEE Communications Surveys & Tutorials* 22.4 (2020), pp. 2283–2314. DOI: 10.1109/COMST.2020.3004197.

[12] Fu Liu et al. "Programmable Metasurfaces: State of the Art and Prospects". In: (2018), pp. 1–5. DOI: 10.1109/ISCAS.2018.8351817.

[13] Huanhuan Yang et al. "A programmable metasurface with dynamic polarization, scattering and focusing control". In: *Scientific Reports* 6 (Oct. 2016). DOI: 10.1038/srep35692.

[14] Christos Liaskos et al. "Design and Development of Software Defined Metamaterials for Nanonetworks". In: *IEEE Circuits and Systems Magazine* 15.4 (2015), pp. 12–25. DOI: 10.1109/MCAS.2015.2484098.

[15] Jie Zhao et al. "A Tunable Metamaterial Absorber using Varactor Diodes". In: *New Journal of Physics* 15 (Apr. 2013), p. 043049. DOI: 10.1088/1367-2630/15/4/043049.

[16] Senglee Foo. "Liquid-crystal reconfigurable metasurface reflectors". In: (2017), pp. 2069–2070. DOI: 10.1109/APUSNCURSINRSM.2017.8073077.

[17] Tie Cui et al. "Coding metamaterials, digital metamaterials and programmable metamaterials". In: *Light: Science & Applications* 3 (Oct. 2014), e218. DOI: 10.1038/lsa.2014.99.

[18] Qingqing Wu and Rui Zhang. "Beamforming Optimization for Intelligent Reflecting Surface with Discrete Phase Shifts". In: *ICASSP 2019 - 2019 IEEE International Conference on Acoustics, Speech and Signal Processing (ICASSP).* 2019, pp. 7830–7833. DOI: 10.1109/ICASSP.2019.8683145.

[19] Wankai Tang et al. "Wireless Communications With Reconfigurable Intelligent Surface: Path Loss Modeling and Experimental Measurement". In: *IEEE Transactions on Wireless Communications* PP (Sept. 2020), pp. 1–1. DOI: 10.1109/TWC.2020.3024887.

[20] Nadege Kaina et al. "Erratum: Shaping complex microwave fields in reverberating media with binary tunable metasurfaces (Scientific Reports)". In: 5 (Jan. 2015). DOI: 10.1038/srep07966.

[21] Qingqing Wu and Rui Zhang. "Intelligent Reflecting Surface Enhanced Wireless Network: Joint Active and Passive Beamforming Design". In: (2018), pp. 1–6. DOI: 10.1109/GLOCOM.2018.8647620.

[22] Peilan Wang et al. "Intelligent Reflecting Surface-Assisted Millimeter Wave Communications: Joint Active and Passive Precoding Design". In: *IEEE Transactions on Vehicular Technology* 69.12 (2020), pp. 14960–14973. DOI: 10.1109/TVT.2020.3031657.

[23] Qingqing Wu and Rui Zhang. "Intelligent Reflecting Surface Enhanced Wireless Network via Joint Active and Passive Beamforming". In: *IEEE Transactions on Wireless Communications* 18.11 (2019), pp. 5394–5409. DOI: 10.1109/TWC.2019.2936025.

[24] Hailiang Xie, Jie Xu, and Ya-Feng Liu. "Max-Min Fairness in IRS-Aided Multi-Cell MISO Systems With Joint Transmit and Reflective Beamforming". In: *IEEE Transactions on Wireless Communications* 20.2 (2021), pp. 1379–1393. DOI: 10.1109/TWC.2020.3033332.

[25] Xianghao Yu, Dongfang Xu, and Robert Schober. "Enabling Secure Wireless Communications via Intelligent Reflecting Surfaces". In: (2019), pp. 1–6. DOI: 10.1109/GLOBECOM38437.2019.9014322.

[26] Frédérique Oggier and Babak Hassibi. "The Secrecy Capacity of the MIMO Wiretap Channel". In: *IEEE Transactions on Information Theory* 57.8 (2011), pp. 4961–4972. DOI: 10.1109/TIT.2011.2158487.

[27] Xiuhong Wei et al. “Codebook design and beam training for extremely large-scale RIS: Far-field or near-field?” In: *China Communications* 19.6 (2022), pp. 193–204. DOI: 10.23919/JCC.2022.06.015.

[28] Abdelrahman Taha, Muhammad Alrabeiah, and Ahmed Alkhateeb. “Enabling Large Intelligent Surfaces With Compressive Sensing and Deep Learning”. In: *IEEE Access* 9 (2021), pp. 44304–44321. DOI: 10.1109/ACCESS.2021.3064073.

[29] George C. Alexandropoulos and Evangelos Vlachos. “A Hardware Architecture For Reconfigurable Intelligent Surfaces with Minimal Active Elements for Explicit Channel Estimation”. In: (2020), pp. 9175–9179. DOI: 10.1109/ICASSP40776.2020.9053976.

[30] Yifei Yang et al. “Intelligent Reflecting Surface Meets OFDM: Protocol Design and Rate Maximization”. In: *IEEE Transactions on Communications* 68.7 (2020), pp. 4522–4535. DOI: 10.1109/TCOMM.2020.2981458.

[31] Yifei Yang et al. “Intelligent Reflecting Surface Meets OFDM: Protocol Design and Rate Maximization”. In: *IEEE Transactions on Communications* 68.7 (2020), pp. 4522–4535. DOI: 10.1109/TCOMM.2020.2981458.

[32] Tobias Lindstrøm Jensen and Elisabeth De Carvalho. “An Optimal Channel Estimation Scheme for Intelligent Reflecting Surfaces Based on a Minimum Variance Unbiased Estimator”. In: (2020), pp. 5000–5004. DOI: 10.1109/ICASSP40776.2020.9053695.

[33] Changsheng You, Beixiong Zheng, and Rui Zhang. “Channel Estimation and Passive Beamforming for Intelligent Reflecting Surface: Discrete Phase Shift and Progressive Refinement”. In: *IEEE Journal on Selected Areas in Communications* 38.11 (2020), pp. 2604–2620. DOI: 10.1109/JSAC.2020.3007056.

[34] Peilan Wang et al. “Compressed Channel Estimation for Intelligent Reflecting Surface-Assisted Millimeter Wave Systems”. In: *IEEE Signal Processing Letters* 27 (2020), pp. 905–909. DOI: 10.1109/LSP.2020.2998357.

[35] Xinying Ma et al. “Joint Channel Estimation and Data Rate Maximization for Intelligent Reflecting Surface Assisted Terahertz MIMO Communication Systems”. In: *IEEE Access* 8 (2020), pp. 99565–99581. DOI: 10.1109/ACCESS.2020.2994100.

[36] Changsheng You, Beixiong Zheng, and Rui Zhang. “Fast Beam Training for IRS-Assisted Multiuser Communications”. In: *IEEE Wireless Communications Letters* 9.11 (2020), pp. 1845–1849. DOI: 10.1109/LWC.2020.3005980.

[37] Samuel M Sherman and Daivd K Barton. *Monopulse principles and techniques.* Artech House, 2011.

[38] *Monopulse Radar*. Jan. 2021. URL: https://en.wikipedia.org/wiki/Monopulse_radar.

[39] Sandeep Gogineni and Arye Nehorai. “Monopulse MIMO Radar for Target Tracking”. In: *IEEE Transactions on Aerospace and Electronic Systems* 47.1 (2011), pp. 755–768. DOI: 10.1109/TAES.2011.5705707.

[40] Do-Jin An and Joon-Ho Lee. “Performance Analysis of Amplitude Comparison Monopulse Direction-of-Arrival Estimation”. In: *Applied Sciences* 10.4 (2020). ISSN: 2076-3417. DOI: 10.3390/app10041246. URL: https://www.mdpi.com/2076-3417/10/4/1246.

[41] Werner Kederer and Jürgen Detlefsen. “Direction of arrival (DOA) determination based on monopulse concepts”. In: *2000 Asia-Pacific Microwave Conference. Proceedings (Cat. No. 00TH8522)*. IEEE. 2000, pp. 120–123.

[42] *Phase-comparison monopulse*. Feb. 2021. URL: `https://en.wikipedia.org/wiki/Phase-comparison_monopulse`.

[43] Fjolla Ademaj et al. “A Spatial Consistency Model for Geometry-Based Stochastic Channels”. In: *IEEE Access* 7 (2019), pp. 183414–183427. DOI: `10.1109/ACCESS.2019.2958154`.

[44] U. Nickel. “Overview of generalized monopulse estimation”. In: *IEEE Aerospace and Electronic Systems Magazine* 21.6 (2006), pp. 27–56. DOI: `10.1109/MAES.2006.1662039`.

[45] Miguel Poveda-García and José Luis Gómez-Tornero. “Ambiguity Resolution in Amplitude-Monopulse Systems Using Broad-Beam Patterns”. In: *IEEE Antennas and Wireless Propagation Letters* 20.4 (2021), pp. 503–507. DOI: `10.1109/LAWP.2021.3055275`.

A

Appendix A

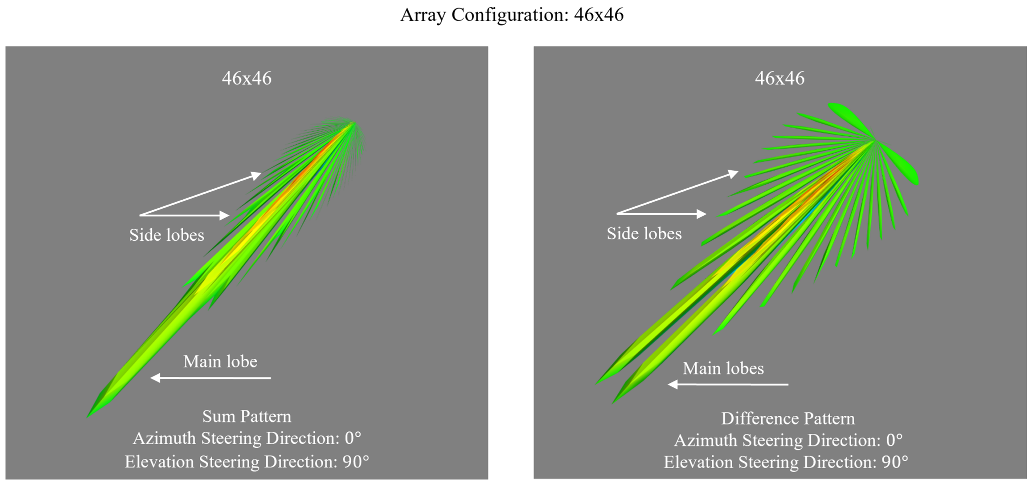

(a) The monopulse sum and difference patterns steered to 0° in the azimuth axis.

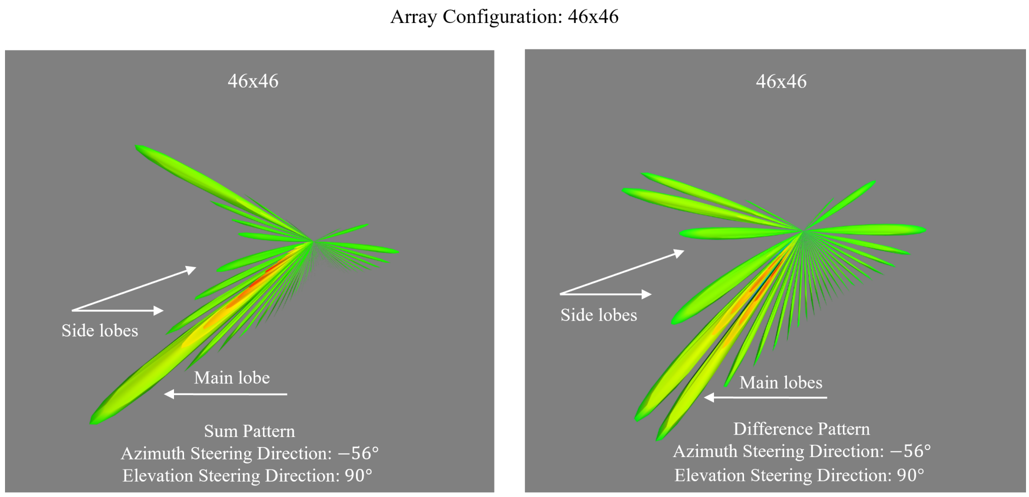

(b) The monopulse sum and difference patterns steered to −56° in the azimuth axis.

Figure A.1: A 3D view of the monopulse sum and difference patterns for the array configuration 46×46.

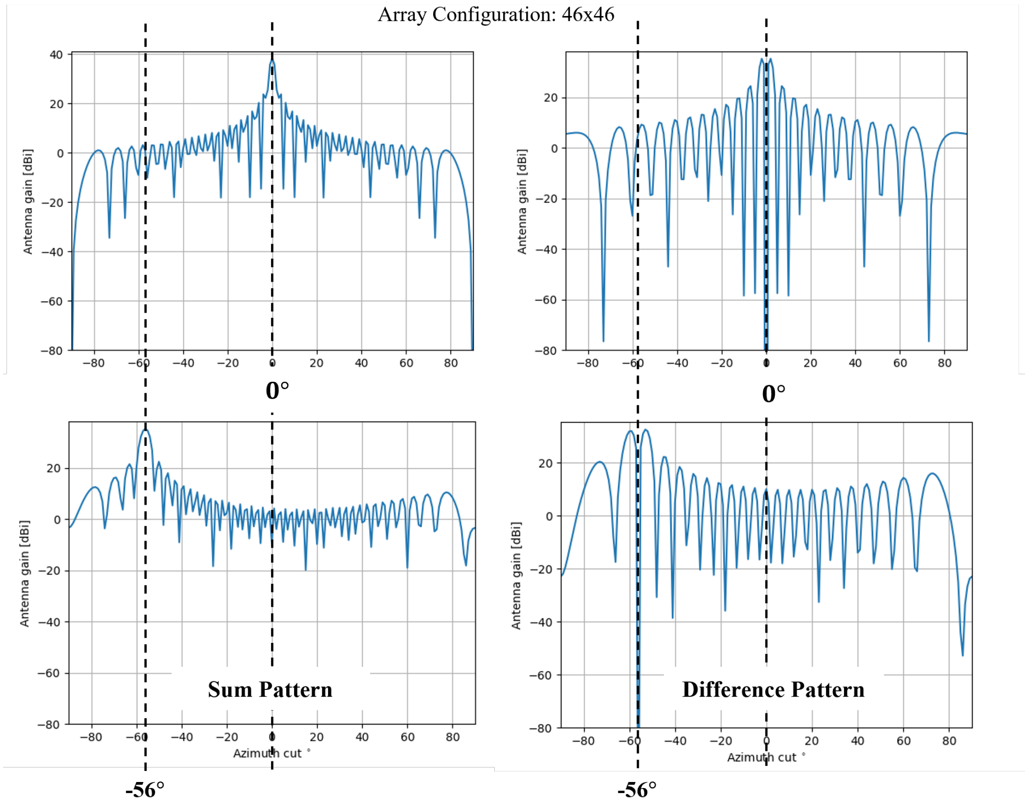

Figure A.2: A 2D view of the monopulse sum and difference patterns for the array configuration 46×46.

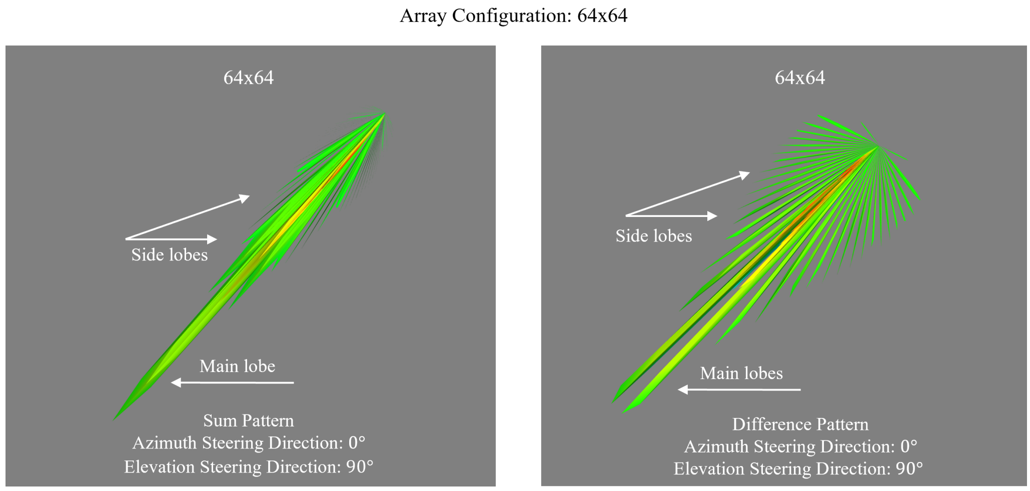

(a) The monopulse sum and difference patterns steered to 0° in the azimuth axis.

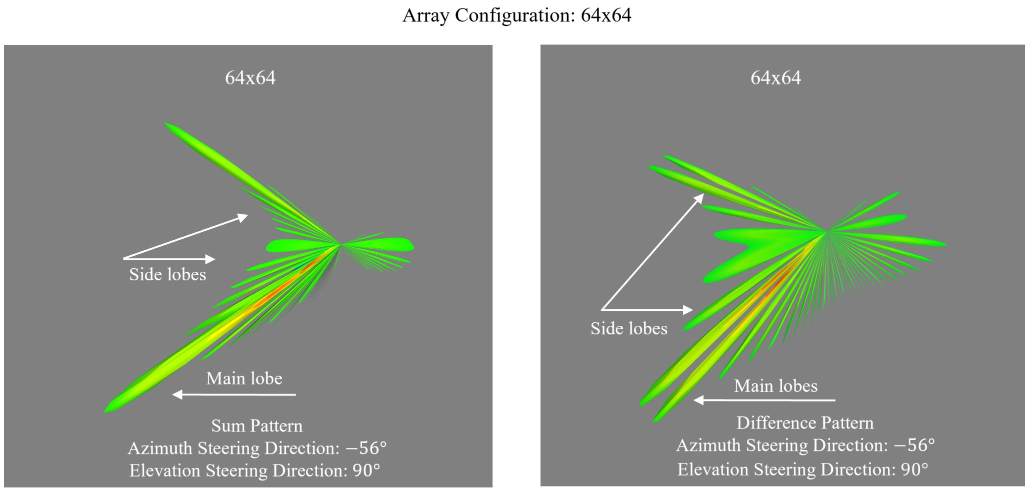

(b) The monopulse sum and difference patterns steered to −56° in the azimuth axis.

Figure A.3: A 3D view of the monopulse sum and difference patterns for the array configuration 64×64.

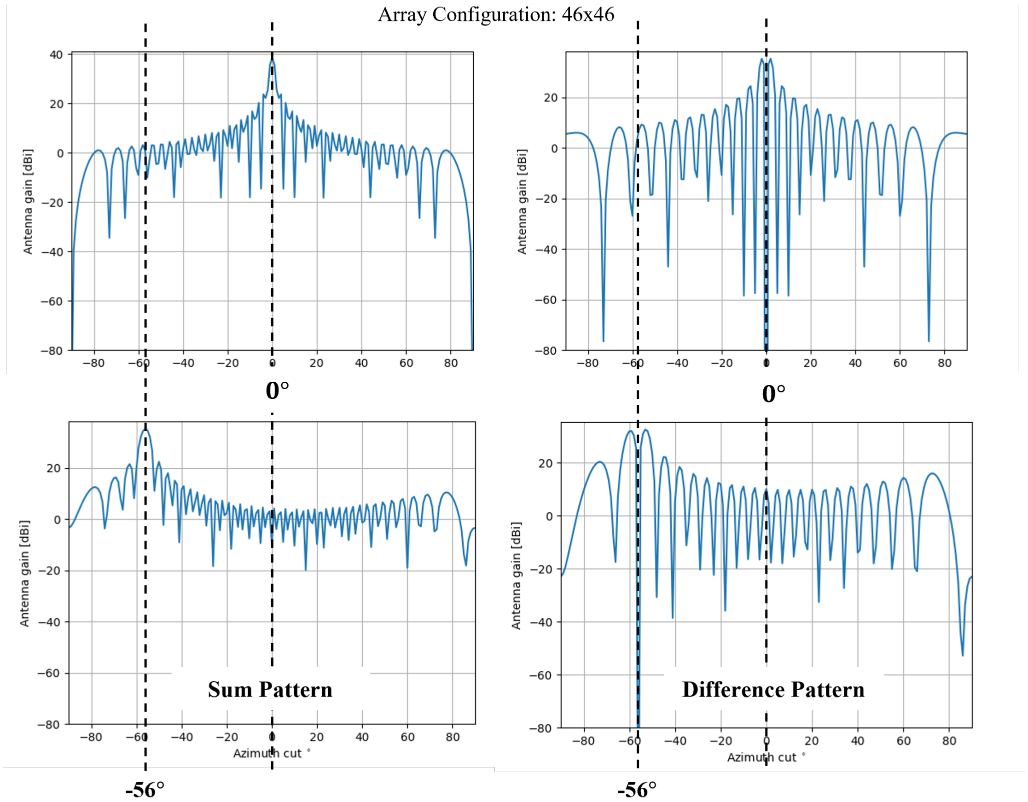

Figure A.4: A 2D view of the monopulse sum and difference patterns for the array configuration 64×64.

B

Appendix B

RX [x y z] [meters]	Azimuth: true direction [degrees]	Azimuth: estimated direction [degrees]	Error [degrees]	Elevation: true direction [degrees]	Elevation: estimated direction [degrees]	Error [degrees]
0 [100. 15. 20]	-53.471	-56.310	2.839	108.959	110.556	1.597
1 [100. 25. 10]	-51.340	-35.184	16.156	104.030	101.034	2.995
2 [100. 50. 6]	-45.000	-48.867	3.867	99.287	108.521	9.234
3 [100. 60. 1.5]	-41.987	-47.335	5.347	90.000	96.560	6.560
4 [100. 82. 5.]	-34.216	-34.606	0.390	110.411	111.057	0.646
5 [100. 98. 7.]	-27.474	-34.799	7.325	101.218	99.369	1.849
6 [100. 110. 13.]	-21.801	-48.867	27.066	105.589	110.556	4.967
7 [100. 125. 17.]	-14.036	-7.125	6.911	107.752	105.376	2.376
8 [100. 137. 30.]	-7.407	-21.306	13.899	109.824	100.204	9.620
9 [100. 145. 35.]	-2.862	-6.560	3.698	110.882	111.057	0.175
10 [100. 158. 40.]	4.574	6.560	1.986	110.411	111.057	0.646
11 [100. 179. 45.]	16.172	7.970	8.203	111.059	97.125	13.934
12 [100. 185. 50.]	19.290	19.799	0.509	111.100	111.057	0.043
13 [100. 193. 2.]	23.268	21.057	2.211	92.861	92.577	0.284
14 [100. 200. 17.]	26.565	30.541	3.976	106.445	99.090	7.354
15 [100. 210. 5.]	30.964	31.592	0.628	100.124	110.807	10.682
16 [100. 220. 3.]	34.992	34.992	0.000	95.693	111.057	15.364
17 [100. 240. 28.]	41.987	35.184	6.803	107.282	109.034	1.752
18 [100. 275. 42.]	51.340	56.310	4.970	113.796	111.057	2.739
19 [100. 290. 2.]	54.462	49.114	5.348	92.749	93.434	0.684
Average Error			**6.117**			**4.698**

Figure B.1: Azimuth and elevation true and estimated angles for the array configuration 32x32.

RX [x y z] [meters]	**Azimuth: true direction** [degrees]	**Azimuth: estimated direction** [degrees]	**Error** [degrees]	**Elevation: true direction** [degrees]	**Elevation: estimated direction** [degrees]	**Error** [degrees]
0 [100. 15. 20]	-53.471	-44.856	8.615	108.959	114.702	5.743
1 [100. 25. 10]	-51.340	-45.000	6.340	104.030	104.574	0.545
2 [100. 50. 6]	-45.000	-45.000	0.000	99.287	99.369	0.082
3 [100. 60. 1.5]	-41.987	-35.375	6.612	90.000	89.141	0.859
4 [100. 82. 5.]	-34.216	-25.174	9.042	98.520	97.407	1.113
5 [100. 98. 7.]	-27.474	-24.938	2.536	101.218	101.034	0.184
6 [100. 110. 13.]	-21.801	-14.842	6.959	105.589	114.938	9.350
7 [100. 125. 17.]	-14.036	-16.436	2.400	107.752	111.554	3.802
8 [100. 137. 30.]	-7.407	-6.277	1.130	109.824	105.110	4.715
9 [100. 145. 35.]	-2.862	-1.146	1.717	110.882	106.436	4.446
10 [100. 158. 40.]	4.574	0.573	4.001	110.411	105.642	4.769
11 [100. 179. 45.]	16.172	9.926	6.246	111.059	114.938	3.880
12 [100. 185. 50.]	19.290	25.174	5.883	111.100	114.938	3.838
13 [100. 193. 2.]	23.268	27.699	4.432	92.861	92.291	0.570
14 [100. 200. 17.]	26.565	24.938	1.627	106.445	109.545	3.100
15 [100. 210. 5.]	30.964	24.938	6.025	100.124	99.369	0.755
16 [100. 220. 3.]	34.992	36.870	1.878	95.693	95.711	0.018
17 [100. 240. 28.]	41.987	46.261	4.273	107.282	114.702	7.420
18 [100. 275. 42.]	51.340	52.958	1.617	113.796	113.989	0.193
19 [100. 290. 2.]	54.462	49.114	5.348	92.749	91.432	1.317
Average Error			**4.334**			**2.835**

Figure B.2: Azimuth and elevation true and estimated angles for the array configuration 46x46.

RX [x y z] [meters]	Azimuth: true direction [degrees]	Azimuth: estimated direction [degrees]	Error [degrees]	Elevation: true direction [degrees]	Elevation: estimated direction [degrees]	Error [degrees]
0 [100. 15. 20]	-53.471	-51.002	2.469	108.959	108.778	0.181
1 [100. 25. 10]	-51.340	-51.002	0.338	104.030	103.225	0.805
2 [100. 50. 6]	-45.000	-45.000	0.000	99.287	99.648	0.361
3 [100. 60. 1.5]	-41.987	-38.834	3.153	90.000	89.714	0.286
4 [100. 82. 5.]	-34.216	-32.822	1.394	98.520	98.531	0.010
5 [100. 98. 7.]	-27.474	-25.408	2.067	101.218	101.310	0.092
6 [100. 110. 13.]	-21.801	-20.556	1.245	105.589	110.807	5.218
7 [100. 125. 17.]	-14.036	-15.376	1.340	107.752	108.263	0.511
8 [100. 137. 30.]	-7.407	-8.250	0.843	109.824	105.376	4.448
9 [100. 145. 35.]	-2.862	-2.577	0.286	110.882	110.807	0.075-
10 [100. 158. 40.]	4.574	5.994	1.420	110.411	108.778	1.633
11 [100. 179. 45.]	16.172	17.745	1.573	111.059	105.376	5.682
12 [100. 185. 50.]	19.290	21.306	2.016	111.100	116.565	5.465
13 [100. 193. 2.]	23.268	24.466	1.198	92.861	92.291	0.570
14 [100. 200. 17.]	26.565	27.248	0.683	106.445	106.172	0.272
15 [100. 210. 5.]	30.964	26.794	4.170	100.124	99.926	0.198
16 [100. 220. 3.]	34.992	35.184	0.192	95.693	95.711	0.018
17 [100. 240. 28.]	41.987	41.669	0.318	107.752	108.263	0.511
18 [100. 275. 42.]	51.340	54.941	3.600	113.796	111.306	2.490
19 [100. 290. 2.]	54.462	51.002	3.460	92.749	92.577	0.173
Average Error			**1.588**			**1.538**

Figure B.3: Azimuth and elevation true and estimated angles for the array configuration 64x64.

DEPARTMENT OF SOME SUBJECT OR TECHNOLOGY
CHALMERS UNIVERSITY OF TECHNOLOGY
Gothenburg, Sweden
www.chalmers.se

AVANCEZ
1829

CHALMERS
UNIVERSITY OF TECHNOLOGY